NASA-CR-194765

INTERIM
IN-34-CR
OCIT
198567
43P

NASA COOPERATIVE AGREEMENT NCCI-22

COMPUTATIONAL FLUID MECHANICS

Progress Report No. 29

For the Period June 15, 1993 to December 14, 1993

(NASA-CR-194765) COMPUTATIONAL FLUID MECHANICS Progress Report No. 29, 15 Jun. - 14 Dec. 1993 (North Carolina State Univ.) 43 p

N94-24859

Unclas

G3/34 0198567

Prepared by

H. A. Hassan
Project Coordinator

Department of Mechanical and Aerospace Engineering
Post Office Box 7910
North Carolina State University
Raleigh, North Carolina 27695-7910

During this period two abstracts were submitted. The first was submitted to the 25th AIAA Fluid Dynamics Conference, while the second was submitted to the 12th AIAA Applied Aerodynamics Conference. Copies of abstracts are enclosed.

References

1. Fenno, C. C., Jr. and Hassan, H. A., "Direct Numerical Simulation of Leading Edge Recaptivity to Sound for Flow Over Parabolic Cylinders".
2. Warren, E. S., Harris, J. E., and Hassan, H. A., "A Transition Model for High Speed Flow".

Direct Numerical Simulation of Leading Edge Receptivity to Sound for Flow Over Parabolic Cylinders

Charles C. Fenno, Jr. [*]
H. A. Hassan [†]
North Carolina State University, Raleigh, North Carolina

Abstract of Paper Proposed for the
AIAA 25th Fluid Dynamics Conference
June 20-23, 1994
Colorado Springs, Colorado

Abstract

The compressible Navier-Stokes equations have been used to compute leading edge receptivity of boundary layers over parabolic cylinders. Natural receptivity at the leading edge was simulated and Tollmien-Schlichting waves were observed to develop in response to an acoustic disturbance, applied through the farfield boundary conditions.

To facilitate comparison with previous work, all computations were carried out at $M_\infty = 0.3$. The spatial and temporal behavior of the flowfields are calculated through the use of finite volume algorithms and Runge-Kutta integration. The results are dominated by strong decay of the Tollmien-Schlichting wave due to the presence of the mean flow favorable pressure gradient. The effects of numerical dissipation, forcing frequency, and nose radius are studied. The Strouhal number is shown to have the greatest effect on the unsteady results.

---

[*] Research Assistant, Mechanical and Aerospace Engineering, Student Member AIAA.
[†] Professor, Mechanical and Aerospace Engineering, Associate Fellow AIAA.

Introduction

The aerospace design process is complicated by the wide range of factors which affect the flight vehicle. Each of these factors, which include propulsion, structures, and aerodynamics, must be considered at each step in the design process. Recent research on the National Aerospace Plane (NASP) project has shown a very high degree of interdependence among these varied design factors. The aerodynamic shape of the vehicle forebody, for example, will act as an inlet compression structure for the propulsion system. Therefore, the importance of a thorough understanding of the flowfield, even though traditionally essential, has now reached an unprecedented priority.

One of the key aspects of the flow is its transition from a stable laminar state to one of turbulence. Important parameters such as drag, skin friction, and heat transfer differ for laminar and turbulent flows. Small changes in the transition location can have significant effects on the overall value of these parameters. Unfortunately, the study of both laminar and turbulent flows have far outpaced the understanding of the transition mechanisms which link them. The transition phenomenon is believed to consist of three stages.[1] The first of these is the transfer of external disturbances into the viscous layer, which has become known as the receptivity problem. Next is the linear growth of these disturbances, and the final stage is the nonlinear breakdown to turbulence. The linear stability theory is well established and was first verified experimentally by Schubauer and Skramstad.[2] Extensions of the original theory to compressible and three dimensional flows have been made and efficient numerical schemes have been developed.[3] Advances in describing the third, nonlinear stage have more recently been made due largely to advances in computational capabilities. Direct numerical simulations of the transition process have been achieved by several authors.[4, 5, 6]

The majority of past numerical and theoretical work in transition, however, has relied upon simplifying assumptions such that temporal and spatial disturbances are considered separately. Furthermore, spectral methods have been extensively employed. These spectral methods are known to have difficulties with discontinuities, such as those found in compressible flows and flows over complex geometries. The present work extends the capabilities of numerical solution of transitional flows by using algorithms in wide use in computational fluid dynamics (CFD) which are capable of solving compressible flowfields. Furthermore, both spatial and temporal simulation is employed. This is an extension of the work by Fenno, Streett and Hassan[7] in which the transitional flow over a flat plate was numerically simulated. Receptivity in that work was of the forced type, behind the leading edge. The more realistic situation of pressure gradient flow and natural leading edge receptivity is addressed in the present work. Lin, Reed and Saric[8] solved the case of incompressible flow over a flat plate with elliptic leading edge, which is characterized by a small region of favorable pressure gradient in the leading edge region, followed by an extended region of adverse pressure gradient. Their receptivity was of the natural type, with the external disturbance provided by an acoustic wave. The work was extended by Buter[9] to include receptivity to freestream vorticity disturbances. Murdock[10] used an incompressible spectral method to study the leading edge receptivity of flat plates to an acoustic wave. He later extended his work to include parabolic cylinders, and thus favorable pressure gradient.[11] The previous four references worked with the incompressible problem. The current interest, however, is within the compressible regime. The objective of this work is therefore to numerically simulate leading edge receptivity of a parabolic cylinder using a compressible numerical scheme. The Mach number considered here is 0.3, for comparisons and validation to the available body of incompressible results.

Numerical Scheme

The governing equations are the two-dimensional, unsteady, compressible Navier-Stokes equations. A finite volume formulation using second order accurate central differencing is employed. The method follows the approach of Jameson, Schmidt and Turkel[12] and integration is by a four stage, modified Runge-Kutta method. Third difference explicit dissipation is used for numerical stability. The dissipation is scaled by the local eigenvalue of the equations. Following [12], the dissipation scaling parameter is

$$\frac{h_{i+\frac{1}{2},j}}{\Delta t} \tag{1}$$

where $h_{i+\frac{1}{2},j}$ is the cell height at $(i+\frac{1}{2},j)$ and Δt is the integration time step. In one dimension, the time step can be written as

$$\Delta t = \Delta t_x = \frac{h_{i+\frac{1}{2},j}}{|u|+a} \tag{2}$$

where u is the velocity in the x direction, a is the speed of sound and, therefore, $|u|+a$ is the maximum eigenvalue in the x direction. Thus the numerical dissipation is scaled to the local eigenvalue. However, in two dimensions,

$$\frac{1}{\Delta t} = \frac{1}{\Delta t_x} + \frac{1}{\Delta t_y} \quad . \tag{3}$$

Simplification of equation (3) leads to

$$\Delta t = \frac{h_{i+\frac{1}{2},j}}{(|u|+a)+(|v|+a)} \quad . \tag{4}$$

Therefore, the isotropic dissipation obtained by using equation (4) for the scaling term given in equation (1) leads to excessive dissipation. Jou et al.[13] have shown significant degradation of the laminar solution if excessive numerical dissipation, such as that described above, is involved. Improved models have been developed which use an anisotropic approach and are are only modestly more costly to solve than the standard scheme.[14, 15] Therefore an anisotropic dissipation model will also be investigated in the present study. This involves substitution of the directional Δt_x shown in equation (2) for Δt in equation (1). Likewise, the y direction dissipation is scaled by Δt_y. This results in a slight increase in required computer resources because both directional time steps have to be either stored or recalculated at each grid location. It should be noted that the various forms of the time step mentioned above are for computation of the numerical dissipation only. The temporal integration time step uses the complete Δt given by equation (4).

The solid wall boundary uses no-slip and adiabatic boundary conditions. Extrapolation is applied at the outflow boundary, while the inflow boundary is handled using locally steady, one-dimensional characteristic theory. The positive half domain is solved and thus, symmetry boundary conditions are applied at the centerline.

The first step in the solution procedure is to discretize the domain such that the relevant flow structures can be resolved. This is achieved through choice of an appropriate grid. The streamwise resolution must be fine enough to resolve the flow gradients in the mean flow near the leading edge. Streamwise grid spacing in this region is one tenth of a nose radius. This spacing requirement was found by numerical experimentation. The grid is stretched to a spacing no larger than one eighth of a disturbance wavelength at the outflow in order to resolve the desired spatial disturbance. In the body normal direction, the traditional rule is to place at least ten points in the viscous boundary layer. In the present method, however, a more rigorous requirement is the need to resolve the unsteady disturbance profiles. These profiles are of the acoustic and instability waves. The acoustic profile can be estimated with the Stokes wave, while the instability profile is estimated by linear theory. Both of these profiles have strong gradients and inflection points in the near wall region. A minimum of 4 to 5 points is placed before this inflection point. A further requirement is the need to resolve the strong mean flow gradient at the leading edge. Grid spacing normal to the leading edge is one hundredth of a nose radius. In the temporal direction, two constraints must be met. These are the need to resolve the temporal frequency and the need to meet numerical stability requirements. The more restrictive of these is the numerical stability.

The next step is to compute a mean flow. For this part of the calculation, temporal accuracy is not needed and the integration is used only to achieve a steady state solution. Therefore, convergence acceleration in the form of local time stepping and residual smoothing is used to hasten the computation.[16] It is extremely important that, for the high Reynolds numbers employed, a solution with smooth second derivatives be obtained.[17]

Once the mean flow is obtained, the unsteady forcing disturbance is determined. The disturbance takes the form

$$\Delta q = \Delta \tilde{q}\, e^{i(\alpha x - \omega t)} \tag{5}$$

where α is the disturbance wavenumber, ω is the frequency, and

$$\Delta \tilde{q} = \begin{bmatrix} \Delta \tilde{u} \\ \Delta \tilde{v} \\ \Delta \tilde{p} \\ \Delta \tilde{\rho} \end{bmatrix} = \begin{bmatrix} \epsilon_o\, u_\infty \\ 0 \\ -\rho_\infty u_\infty \Delta \tilde{u} \\ -\frac{\rho_\infty}{\gamma p_\infty} \Delta \tilde{p} \end{bmatrix} \tag{6}$$

where ϵ_o is the specified disturbance amplitude. Equation (6) is obtained from the one dimensional, inviscid conservation of mass and momentum equations and the definition of the speed of sound.

The fourth and final step involves superimposing the disturbance on the freestream at the inflow boundary of the computation domain. Thus a disturbed property, q, is written as

$$q = Q_\infty + \Delta q \tag{7}$$

where Q_∞ represents the freestream value. This property becomes the inflow value used in the characteristic boundary conditions. The governing equations are then integrated in a time accurate manner, allowing the disturbance to continually propagate into the flow. Once the disturbance has penetrated the entire field and moved through the outflow boundary, sampling of the desired properties is performed.

Results and Discussion

Steady Results

Results are presented for a Mach number of 0.3 such that comparisons can be made with the linear disturbance theory and other numerical results in the incompressible regime. The problem is modeled after that of Murdock[11] and the nose radius Reynolds number is set at $R_n = 1 \times 10^3$. A value of $\kappa = 2 \times 10^{-3}$ for the coefficient of third difference explicit damping was found to be sufficient to suppress odd-even point decoupling of the solution. The isotropic dissipation defined using equation (4) in equation (2) was initially used. The outflow boundary was set to $R_s = 5 \times 10^5$. A first order outflow extrapolation boundary condition based on Taylor series was applied along the grid lines. The farfield boundary was placed at $x = -4L$ upstream of the leading edge and $y = 566\delta$ above the body at the outflow. The length of the body within the computational domain is denoted by L, and δ is the boundary layer thickness at the outflow boundary. The grid size was 416×352, which results in a resolution of between 374 cells per expected TS wavelength at the nose to 8 cells per wavelength at the outflow. The normal resolution uses a 1.65 percent stretching from a minimum spacing of $y = \delta/35$, which places 29 points in the boundary layer. The results of the steady state solution are shown in figure 1. The figure shows the surface vorticity defined as

$$g = -\Omega \, \frac{\xi^2 + \eta^2}{\xi} \tag{8}$$

where Ω is the nondimensional vorticity and (ξ, η) represent the grid coordinates. This parameter is shown vs. the log of ξ, and compares well with the results of Davis.[18]

Unsteady Results

The unsteady disturbance was placed on the farfield boundary conditions and the integration was continued. This part of the computation does not use the convergence acceleration methods which were used for the steady state computation. The nondimensional disturbance frequency was set to $F = 56 \times 10^{-6}$. This is defined as

$$F = \frac{\omega \nu}{u_\infty^2} \tag{9}$$

where ω is the frequency, ν is the kinematic viscosity and u_∞ is the freestream velocity. The amplitude of the disturbance was set to $\epsilon_o = 2 \times 10^{-2}$. This is of the same order of magnitude used by Buter and Reed[19], who studied receptivity flow over blunt bodies and found the results to be linear up to forcing amplitudes of 4.2×10^{-2}. They attributed this to the favorable pressure gradient damping effect.

The solution is compared to the results of Murdock[11] in figure 2. The temporal Fourier amplitude at the input frequency is plotted against the streamwise Reynolds number at a constant distance from the solid boundary given by a Reynolds number of $R_r = 196$. Qualitative similarity is seen between the present method and Murdock's spectral method results. The amplitudes show an initial strong spike near the nose, followed by a decay and a relatively constant value over most of the body. Murdock maintains that the magnitude of the envelope about the mean is associated with the Tollmien-Schlichting wave.[10, 11]

The instability wave profiles are shown in figure 3, normalized by the edge value of the total fluctuation and plotted against η_B, the Blasius similarity parameter. The instability fluctuation is denoted by a double prime to distinguish it from the total fluctuation. With the exception of the first station at $R_s = 1 \times 10^4$, the instability profiles are seen to take the characteristic dual lobe shape predicted by linear theory. The overall shape is seen to change from approximately equal magnitudes in both lobes to a dominant magnitude in the lower lobe. At about $R_s = 7 \times 10^4$, the upper lobe has been reduced to insignificance. This single lobe shape is then seen to persist downstream. The instability fluctuation is seen to grow from about 10 percent of the total fluctuation at $R_s = 1 \times 10^4$ to almost 30 percent at $R_s = 8 \times 10^4$. For comparison, the results of linear theory are shown in figure 4. Linear theory predicts growth rates, but not absolute magnitude. Thus, the profiles are normalized by their peak value. The different profiles were obtained by using the mean flow profiles at different streamwise stations obtained from the present method to obtain solutions using the linear theory code described in [17]. The linear theory produced similar profiles, as expected, for stations aft of $R_s = 4 \times 10^4$, but produced a differing profile at $R_s = 2 \times 10^4$. This is most likely due to the assumption of parallel flow used by the method, which is not valid in the leading edge region. The peak value is at a height of $\eta_B \approx 1$ for the theoretical profiles, whereas the present method profiles reach their peak at $\eta_B \approx 0.6$. The highly two-dimensional leading edge flow is also the most likely reason for the nonconforming profile shape at $R_s = 1 \times 10^4$ calculated by the present method and shown in figure 3. Furthermore, there is some region at the leading edge where the energy transfer between the long and short wavelength modes is occurring, and the idea of the acoustic and instability waves existing as separate waveforms can not be defended. Therefore no attempt should be made to analyze them separately. Goldstein[20] argues that in the neighborhood of the leading edge, defined as

$$x \leq O\left(\frac{u_\infty}{\omega}\right) \quad , \tag{10}$$

the flow cannot be described as a double-layer structure of a Stokes wave and eigensolutions of the Orr-Sommerfeld equation. In this region, the long wavelength free stream disturbance is undergoing a wavelength reduction process by the non-parallel mean flow effects until the wavelength matches the Tollmien-Schlichting wavelength. Beyond this region, the disturbance wavelength is constant. In terms of the Reynolds number. and using the flow parameters of the present work. the limiting length in equation (10) can be expressed as

$$R_s \leq \mathcal{O}\left(1.8 \times 10^4\right) \quad . \tag{11}$$

which is in close agreement with the point where the uncharacteristic disturbance profile shape shown in figure 3 gives way to the proper shape.

The maximum instability fluctuation of the momentum is shown in figure 5. In the figure, the maximum amplitude is determined over one period of the disturbance in time and also over the body normal direction. This yields a streamwise distribution. Three zones can be distinguished. The initial zone is very near the leading edge and is characterized by a sharp drop in amplitude. The next zone extends to about $R_s = 7 \times 10^4$ and indicates a strong increase in amplitude. The final zone extends to the outflow and shows a relatively constant amplitude with a long wavelength oscillation. These three zones correspond to the characteristic profile shapes given in figure 3. The first zone is associated with the profile at $R_s = 1 \times 10^4$ where the concept of separating the acoustic and instability waves is most likely not valid. The second zone is associated with the characteristically shaped instability profiles for $1 \times 10^4 < R_s < R_s = 7 \times 10^4$. The final zone, extending over the rest of the domain, is identified by the single lobe profile shown in the last profile of figure 3 for $R_s = 7 \times 10^4$. Although the distribution shown in figure 5 is useful for identifying the zones described above, the quantitative amplitude information it offers must be treated as suspect due to the somewhat crude wave separation technique that was necessarily used to obtain it. The Stokes wave. however, is the best approximation of the acoustic signature that has been determined.

The next step in the analysis is to determine the wavenumber of the computed instability wave. Figure 6 shows the instantaneous momentum fluctuation vs. the streamwise direction at a normal distance defined by $\eta_B = 0.6$. This distance from the wall is where the largest fluctuation is seen in the instability profiles of figure 3. The long wavelength acoustic fluctuation is clearly seen in the figure. while a shorter length oscillation of much smaller amplitude is seen in the leading edge region. The smaller amplitude can be estimated as being about an order of magnitude smaller than the acoustic amplitude. This is in agreement with the magnitude of the instability profiles of figure 3. This shorter lengthscale oscillation is seen to be strongly damped beyond about $R_s = 5 \times 10^4$.

The data series length represented by figure 6 is necessarily truncated with respect to the number of wavelengths. The acoustic wavelength is approximately equal to the body length. thus only one wavelength is available for analysis. Furthermore, figure 6 indicates the existence of the instability wave for only a few wavelengths. These restrictions cause difficulties in the ability of traditional Fourier analysis techniques to resolve wavenumbers and amplitudes.[21] It was therefore necessary to use a technique better suited to the analysis of truncated series, the Maximum Entropy Method (MEM).[22, 23, 24] Corke[21] maintains that this method is best used to detect the existence of various modes, rather than extract quantitative data. Figure 7 shows the results of the MEM when applied to the data series defined by figure 6. The power spectrum clearly displays three peaks. The first peak is at a wavenumber very close to the input acoustic wavenumber. The last peak is very close to the value predicted by linear stability theory, illustrating the existence of the higher wavenumber Tollmien-Schlichting wave. The middle peak is associated with the numerical window function used in the analysis and is not indicative of any physical process.

The existence of the TS wave is thus illustrated by identifying its wavenumber, at least qualitatively as seen in figure 7, and its profile shape, seen in figure 3. Its amplitude can be deduced from figure 6 as approximately an order of magnitude smaller than the acoustic wave and strongly damped in the streamwise direction. There are several possible sources of this damping. Since the TS wave propagation was successfully simulated using the present method for flat plate flows[7], complete with amplification and decay in the proper regions, it is reasonable to investigate the fundamental differences between flat plate flow and parabolic cylinder flow for the cause of the present TS wave damping. The first difference is the surface curvature. It is known that a convex surface has a stabilizing effect on the stability of a boundary layer, as compared to the flat plate.[25, 26] However, Schlichting[26] also notes that this influence is very small if the ratio of the boundary layer thickness to the radius of curvature is small, as in the present case. Reshotko,[25] in his review of boundary layer stability refers to early work of Liepmann[27] who observed that transition on convex surfaces occurs at about the same Reynolds number as on flat plates. Therefore, while the curvature may be contributing to the TS wave damping, it is not believed to be a strong effect, especially since the curvature is small away from the leading edge. Another factor which must be mentioned is the presence of a favorable pressure gradient. This has a much stronger effect on the stability of the boundary layer.[25, 26, 28, 29] The exploitation of a favorable pressure gradient as a transition control mechanism has even been studied.[30] Figure 8 compares the pressure gradient of the parabolic cylinder and the flat plate mean flows of [7]. As expected, the pressure gradient is seen to be much more favorable for the parabolic cylinder until approximately $R_s = 1 \times 10^5$, beyond which the results are essentially the same. This is well beyond the point where the short wavelength oscillation is observed in figure 6. This is strong support, therefore, for the pressure gradient as a leading cause of the instability wave damping observed.

Dissipation Model Study

The results for the parabolic cylinder reported above used the two dimensional time step defined by equation (4) to scale the numerical dissipation. The anisotropic correction discussed following equation (4) was applied to the dissipation at this point. The steady state flow was recalculated and the temporally accurate integration was conducted to 10 disturbance periods using an input disturbance amplitude of $\epsilon_o = 2 \times 10^{-2}$, as in the previous case. The acoustic amplitude at the body is $\epsilon_e = 8.8 \times 10^{-3}$, or 44 percent of the input amplitude. Previously, this was $\epsilon_e = 1.3 \times 10^{-3}$, or 6.5 percent. Figure 9 shows the TS profile for the two formulations at $R_s = 5 \times 10^4$. Only a small change is seen in the instability response which can easily be a result of the subtle changes in the mean flow. Thus, the improved damping formulation allows more of the input disturbance amplitude to reach the body, but the TS response remains essentially unchanged.

Nose Radius Study

Hammerton and Kerschen,[31] utilizing asymptotic methods, have shown the level of receptivity of a parabolic cylinder to freestream acoustic waves to be dramatically increased for lower Strouhal number. The Strouhal number is defined as

$$S = F\,R_n \tag{12}$$

and represents the ratio of nose radius to characteristic disturbance lengthscale. Therefore, to improve the TS response, the body nose radius was decreased from $R_n = 1000$ to $R_n = 243$. The Strouhal number is thus reduced from $S = 5.6 \times 10^{-2}$ to $S = 1.36 \times 10^{-2}$.

The results of the unsteady computation show significant differences as compared to the $R_n = 1000$ case. Figure 10 shows the computed instability profiles. The streamwise distributions are compared in figure 11. As before, the first profile station at $R_s = 1 \times 10^4$ shows no characteristic instability shape and falls in the first zone of sharp amplitude decay in figure 11. The next two profiles fall within the second zone and show an initial growth of amplitude followed by a decay. Previously, only a growth was seen. Profiles between $R_s = 7 \times 10^4$ and $R_s = 9 \times 10^4$ develop a small lower lobe and a dominant upper lobe and lie within the third zone in figure 11. This third zone is also characterized by amplitude growth followed by decay. The final profile at $R_s = 1.1 \times 10^5$ shows another shift of magnitude from the upper to lower lobe and again begins an amplitude growth which continues through the outflow boundary. This repeating growth and decay cycle was not seen previously for the $R_n = 1000$ case. That case does, however, show the growth portion of the first cycle before settling into a persistent single lobe shape.

To explain the unusual behavior for this case, the mean flow pressure gradient distribution is displayed in figure 12 along with the distributions for the previous $R_n = 1000$ case, and for the flat plate case. The pressure gradient, while still favorable, is much less so for the present case. This is a very convincing argument for the importance of the pressure gradient in the stability of the boundary layer. Whereas before no discernible TS behavior was seen beyond $R_s = 7 \times 10^4$, here the TS profiles continue their characteristic shape to the outflow of the domain at $R_s = 1.2 \times 10^5$.

Frequency Study

The previous case involved a change in both the pressure gradient and the Strouhal number. To determine which of these changes is dominant, the final study is of a higher input frequency, $F = 230 \times 10^{-6}$ and uses the $R_n = 243$ geometry. This frequency and geometry were chosen in order to maintain the same Strouhal number, $S = 5.6 \times 10^{-2}$, which was used previously with the larger nose radius and lower frequency. Furthermore, a higher frequency will produce a less stable boundary layer, as predicted by the upstream shifting of the branch points by linear theory. Furthermore, Reed, Lin and Saric[8] have numerically shown a greater TS wave amplitude for higher frequency. The amplitude distribution is shown in figure 13 and shows very similar trends as for the lower frequency, larger nose radius results. This includes the initial amplitude drop, followed by an amplitude increase with the TS profile development, and then followed by a relatively unchanging amplitude for the remainder of the domain. The difference between the cases is in the range of R_s where the various behaviors are seen. Previously, the TS profiles were in the range $2 \times 10^4 \leq R_s \leq 7 \times 10^4$, whereas in this case the range is $6 \times 10^3 \leq R_s \leq 1.6 \times 10^4$. Thus, at a given R_s, the higher frequency yields higher TS amplitudes. Note, however, that in terms of the nose radius, as seen in figure 14, both cases are very similar with the TS profile zone falling between 20 and 70 nose radii aft of the leading edge. The case which used $S = 1.36 \times 10^{-2}$, continues to follow its unique trends under the R_n normalization, however. This serves to underline the importance of the Strouhal number, rather than either the nose radius or frequency alone, as the important similarity parameter for leading edge receptivity studies.

Concluding Remarks

The objective of the present study was met in that the compressible Navier-Stokes equations, using a finite volume formulation, have been successfully used to compute leading edge receptivity of boundary layer over a parabolic cylinder. Natural leading edge receptivity was simulated and Tollmien-Schlichting waves were observed to develop in response to an acoustic disturbance, applied through the farfield boundary conditions. The Tollmien-Schlichting waves which developed compared qualitatively with the results of linear disturbance theory. The wavenumber of the TS waves was determined using the Maximum Entropy Method (MEM) and compared well with the wavenumber predicted by linear stability theory.

The TS waves which were observed in the simulation were characterized by a strong amplitude attenuation in the spatial direction and the source of the attenuation was investigated. An anisotropic formulation of the artificial dissipation model was implemented. This allowed more of the input disturbance amplitude to reach the body, but the amplitudes were found to scale linearly to the original solution. Thus, the numerical dissipation was not found to have a significant effect on the strong TS wave damping.

A smaller nose radius parabolic cylinder was employed and significant changes were seen in the unsteady results. To determine whether the changes were due to the resulting change in pressure gradient or to the interaction of the acoustic wave with the smaller nose radius, a higher frequency case was computed using the smaller nose radius cylinder. The frequency was chosen such that the Strouhal number, or ratio of nose radius to disturbance wavelength, was the same as for the lower frequency, larger nose radius case. The solution was found to compare similarly to the original lower frequency solution in terms of the TS wave damping. Thus, it is concluded that the parameter which affects the development of the TS waves is the Strouhal number, rather than the frequency or nose radius alone. The damping of the TS wave for the lower Strouhal number computation was, however, still significant. Therefore, the stabilizing effect of the favorable pressure gradient continued to have a dominant effect on the development of the TS wave.

The present method, utilizing the compressible Navier-Stokes equations and a finite volume scheme, has been shown to be successful in simulating leading edge receptivity. The method has been validated in the nearly incompressible regime and for relatively simple geometries. With this accomplished, the extension of the method to higher Mach number flows and complex geometries is now possible. This capability has not previously been available.

Acknowledgments

This work is supported in part by NASA's Cooperative Agreement NCCI-22 and the Mars Mission Research Center funded by NASA Grant NAGW-1331. The computer time was provided by the North Carolina Supercomputing Center and NASA's National Aerodynamic Simulation Program. The many helpful conversations with Dr. Craig L. Streett of NASA Langley Research Center and Dr. N. Chokani of North Carolina State University are greatly appreciated.

References

[1] Heinrich. R.A., Choudhari. M. and Kerschen. E.J. "A Comparison of Boundary Layer Receptivity Mechanisms." AIAA Paper 88-3758, 1988.

[2] Schubauer. G.B. and Skramstad, H.K. "Laminar Boundary-Layer Oscillations and Stability of Laminar Flow." *Journal of the Aeronautical Sciences*, 14(2), 1947.

[3] Malik, M.R. and Orszag. S.A. "Linear Stability of Three-Dimensional Compressible Boundary Layers." *Journal of Scientific Computing*, 2(1). 1987.

[4] Fasel, H.F., Rist, U. and Konzelmann, U. "Numerical Investigation of the Three-Dimensional Development in Boundary Layer Development." AIAA Paper 87-1203, 1987.

[5] Zang, T.A., Krist. S.E. and Hussaini, M.Y. "Resolution Requirements for Numerical Simulations of Transition." NASA CR-181799, 1989.

[6] Spalart. P.R. and Yang. K.S. "Numerical Study of Ribbon-Induced Transition in Blasius Flow." *Journal of Fluid Mechanics*. 178:345–365. 1987.

[7] Fenno, C.C., Streett, C.L. and Hassan, H.A. "Use of Finite Volume Schemes for Transition Simulation." AIAA Paper 91-0743, 1991.

[8] Reed, H.L., Lin, N. and Saric. W.S. "Boundary Layer Receptivity to Sound: Navier-Stokes Computations." *Applied Mechanics Reviews*. 43. Part 2(5), 1990.

[9] Buter, T.A. "Numerical Simulation of Leading-Edge Receptivity to Freestream Vorticity." Ph.D. Dissertation. Arizona State University, 1992.

[10] Murdock, J.W. "The Generation of a Tollmien-Schlichting Wave by a Sound Wave." *Proceedings of the Royal Society of London. Series A*, 372:517–534, 1980.

[11] Murdock, J.W. "Tollmien-Schlichting Waves Generated by Unsteady Flow Over Parabolic Cylinders." AIAA Paper 81-0199, 1981.

[12] Jameson, A., Schmidt, W. and Turkel, E. "Numerical Solutions of the Euler Equations by Finite Volume Methods Using Runge-Kutta Time Stepping Schemes." AIAA Paper 81-1259, 1981.

[13] Jou, W.H., Wigton, L.B., Allmaras, S.R., Spalart, P.R. and Yu, N.J. "Towards Industrial-Strength Navier-Stokes Codes." In *Fifth Symposium on Numerical and Physical Aspects of Aerodynamic Flows.* California State University, 1992.

[14] Swanson, R.C. and Turkel, E. "Artificial Dissipation and Central Difference Schemes for the Euler and Navier-Stokes Equations." AIAA Paper 87-1107, 1987.

[15] Martinelli, L. and Jameson, A. "Validation of a Multigrid Method for the Reynolds Averaged Equations." AIAA Paper 88-0414, 1988.

[16] Turkel, E. "Acceleration to a Steady State for the Euler Equations." NASA CR-172398, 1984.

[17] Macaraeg, M.G., Streett, C.L. and Hussaini, M.Y. "A Spectral Collocation Solution to the Compressible Stability Eigenvalue Problem." NASA TP-2858, 1988.

[18] Davis, R.T. "Numerical Solution of the Navier-Stokes Equations for Symmetric Laminar Incompressible Flow Past a Parabola." *Journal of Fluid Mechanics*, 51, Part 3:417–433, 1972.

[19] Buter, T.A. and Reed, H.L. "Numerical Investigation of Receptivity to Freestream Vorticity." AIAA Paper 93-0073, 1993.

[20] Goldstein, M.E. "The Evolution of Tollmien-Schlichting Waves Near A Leading Edge." *Journal of Fluid Mechanics*, 127:59–81, 1983.

[21] Toman, K. "The Spectral Shifts of Truncated Sinusoids." *Journal of Geophysical Research*, 70(7):1749–1750, 1965.

[22] Ulrych, T.J. "Maximum Entropy Power Spectrum of Truncated Sinusoids." *Journal of Geophysical Research*, 77(8):1396–1400, 1972.

[23] Ulrych, T.J., Smylie, D.E., Jensen, O.G. and Clarke, G.K.C. "Predictive Filtering and Smoothing of Short Records by Using Maximum Entropy." *Journal of Geophysical Research*, 78(23):4959–4964, 1973.

[24] Corke, T.C., Shakib, F. and Nagib, H.M. "Mode Selection and Resonant Phase Locking in Unstable Axisymmetric Jets." *Journal of Fluid Mechanics*, 223:253–311, 1991.

[25] Reshotko, E. "Boundary-Layer Stability and Transition." *Annual Review of Fluid Mechanics*, 8:311–349, 1976.

[26] Schlichting, H. *Boundary-Layer Theory.* McGraw-Hill, New York, 7th edition, 1979.

[27] Liepmann, H.W. "Investigation of Laminar Boundary Layer Stability and Transition on Curved Boundaries." NACA Wartime Report W-107, 1943.

[28] White, F.M. *Viscous Fluid Flow.* McGraw-Hill, New York, 1974.

[29] Saric, W.S. and Nayfeh, A.H. "Nonparallel Stability of Boundary-Layer Flows." *Physics of Fluids*, 18(8), 1975.

[30] Reshotko, E. "Control of Boundary Layer Transition." AIAA Paper 85-0562, 1985.

[31] Hammerton, P.W. and Kerschen, E.J. "Effect of Nose Bluntness on Leading-Edge Receptivity." In *Proceedings of Transition and Turbulence Workshop.* NASA-LaRC, 1991.

Figures

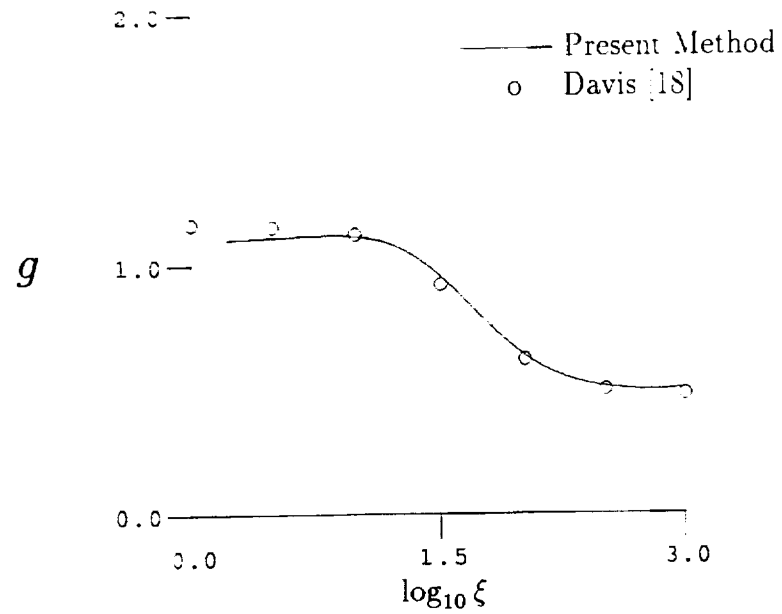

Figure 1: Surface Vorticity Parameter vs. Streamwise Grid Coordinate for Present Method and Davis(1972)

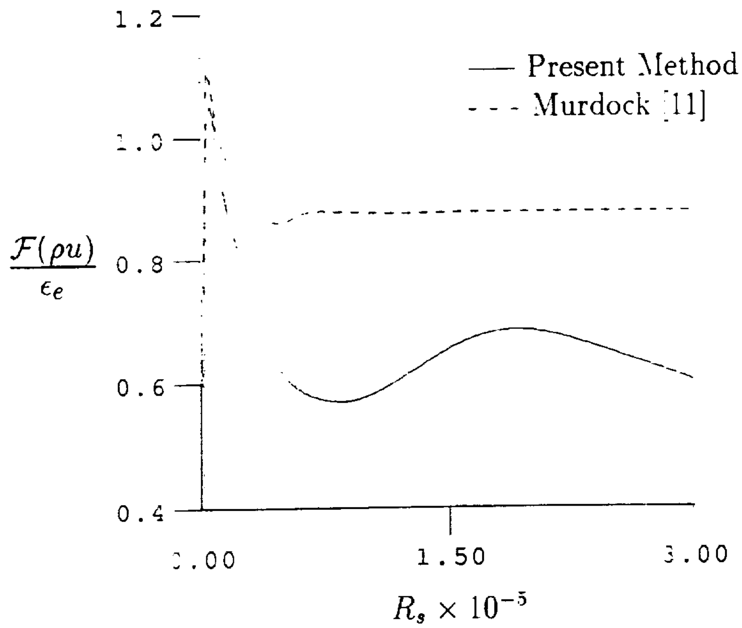

Figure 2: Fourier Amplitude of Streamwise Momentum vs. Reynolds Number for Present Method and Murdock(1981). $R_r = 196$

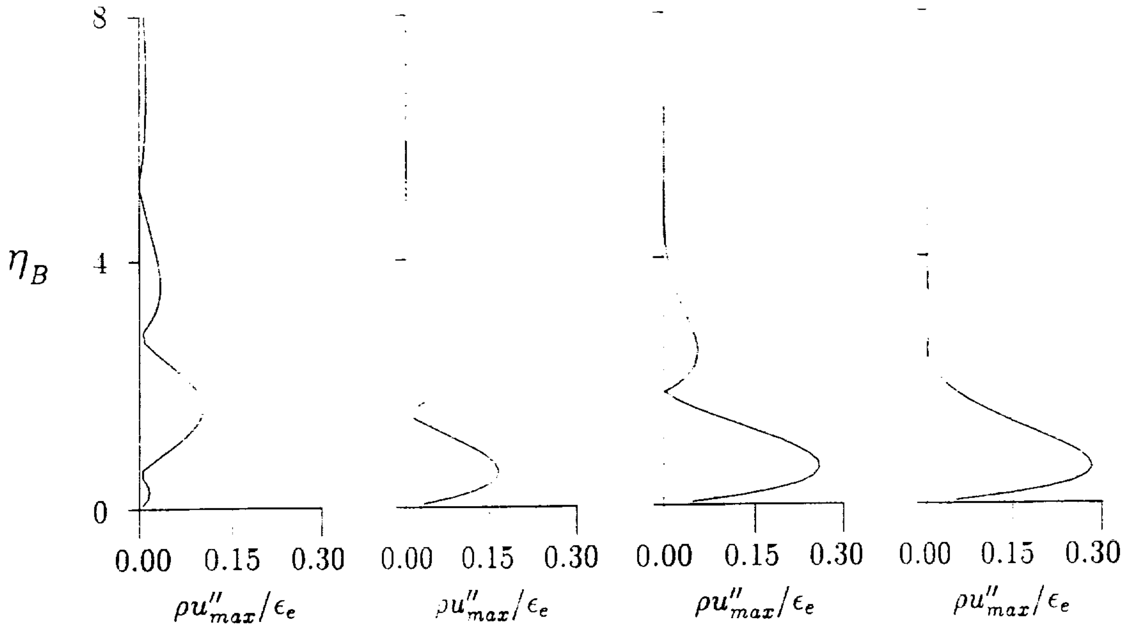

Figure 3: Maximum Streamwise Momentum Fluctuation Profiles Minus Stokes Wave for $R_n = 1000$, $F = 56 \times 10^{-6}$. $1 \times 10^4 \leq R_s \leq 7 \times 10^4$

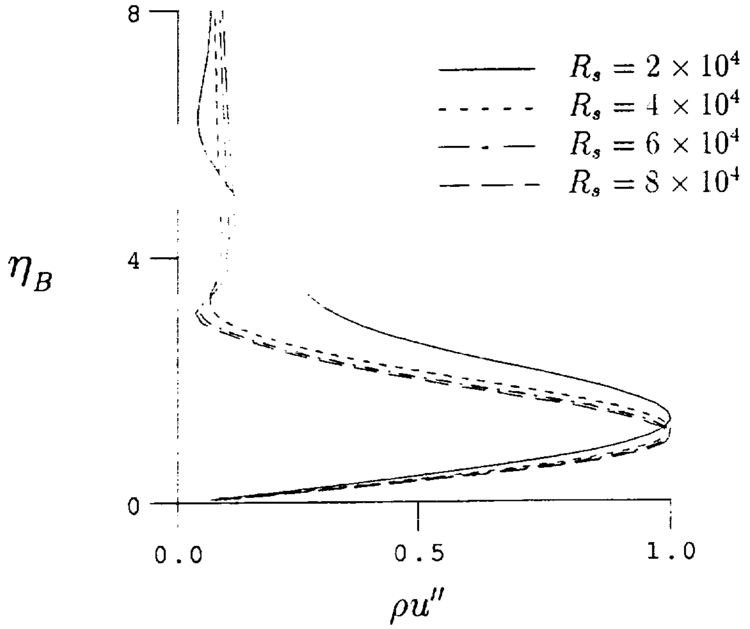

Figure 4: Disturbance Eigenfunctions From Linear Theory

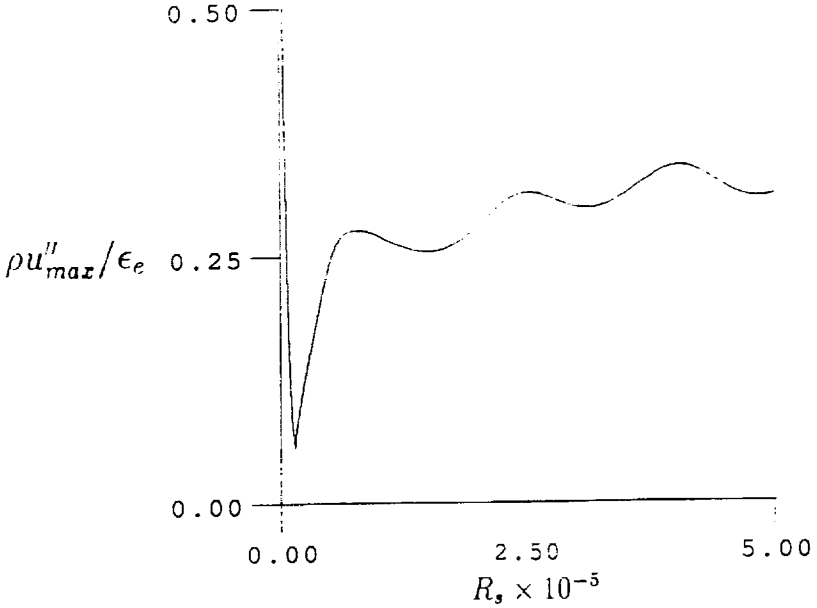

Figure 5: Maximum Streamwise Momentum Fluctuation Minus Stokes Wave vs. Reynolds Number

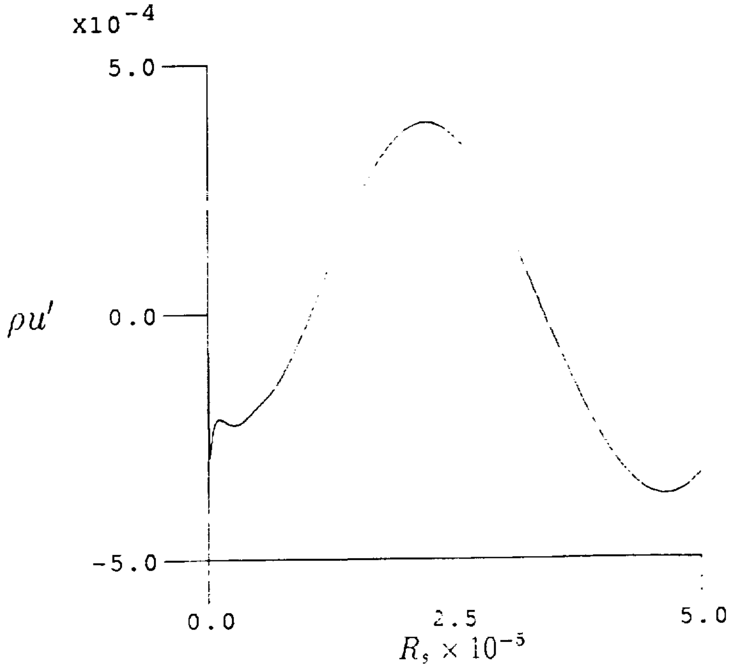

Figure 6: Instantaneous Momentum Fluctuation vs. Reynolds Number for Parabolic Cylinder. $\eta_B = 0.6$

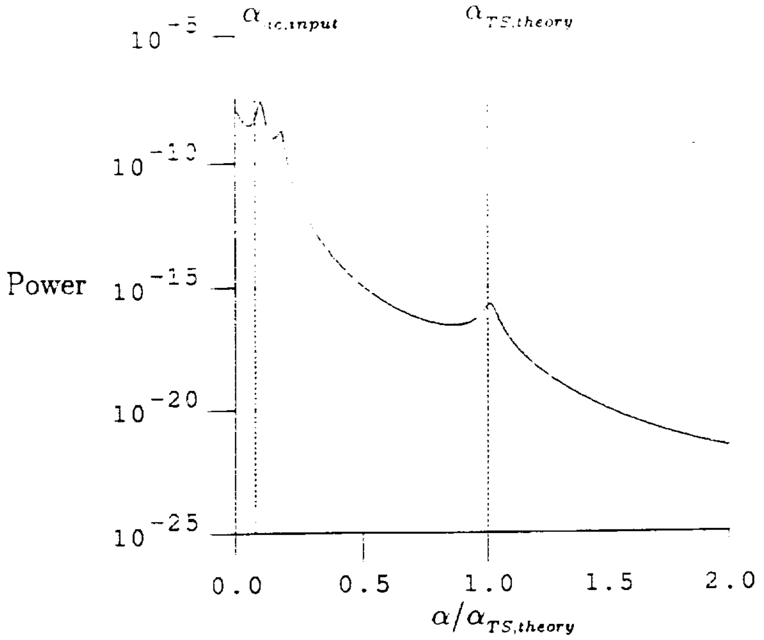

Figure 7: Fourier Power Spectrum of Spatial Streamwise Momentum Fluctuation

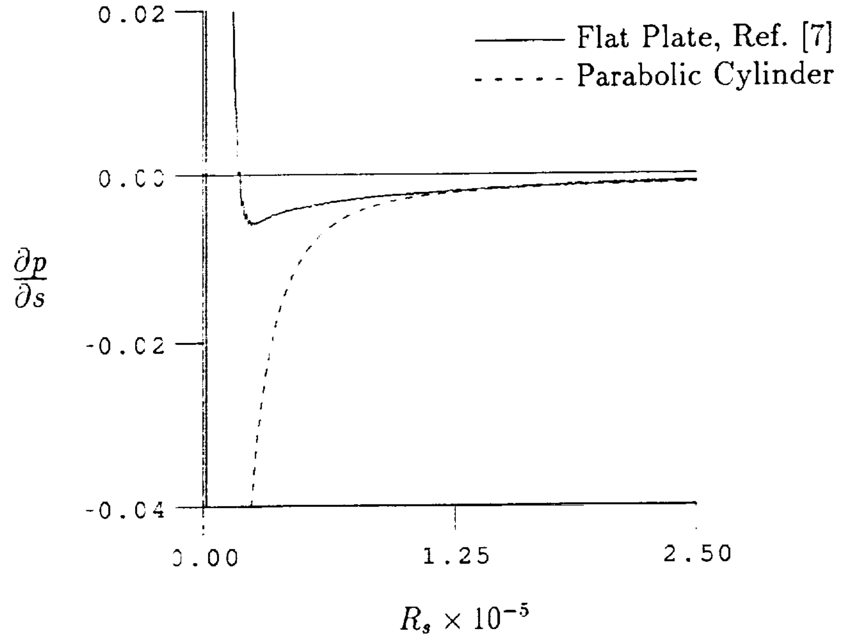

Figure 8: Mean Flow Pressure Gradient vs. Reynolds Number for Flat Plate and Parabolic Cylinder

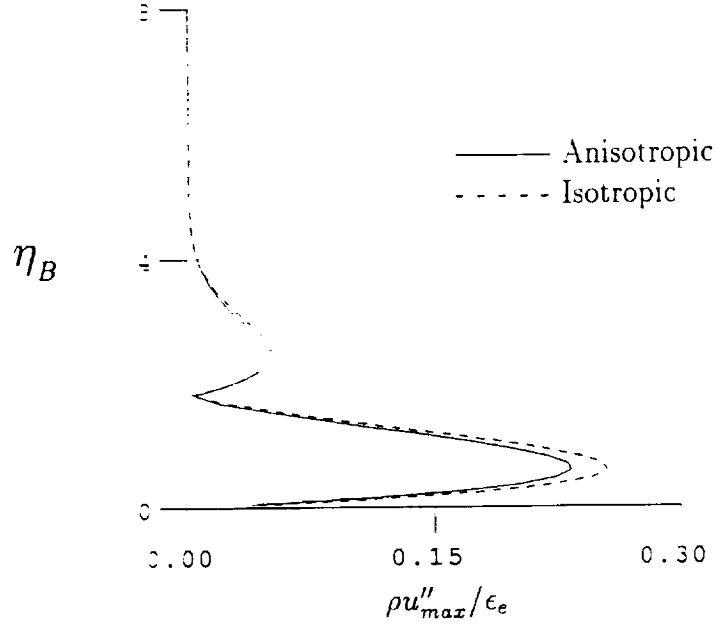

Figure 9: Maximum Streamwise Momentum Fluctuation Profiles Minus Stokes Wave for Isotropic and Anisotropic Artificial Dissipation Models. $R_s = 5 \times 10^4$

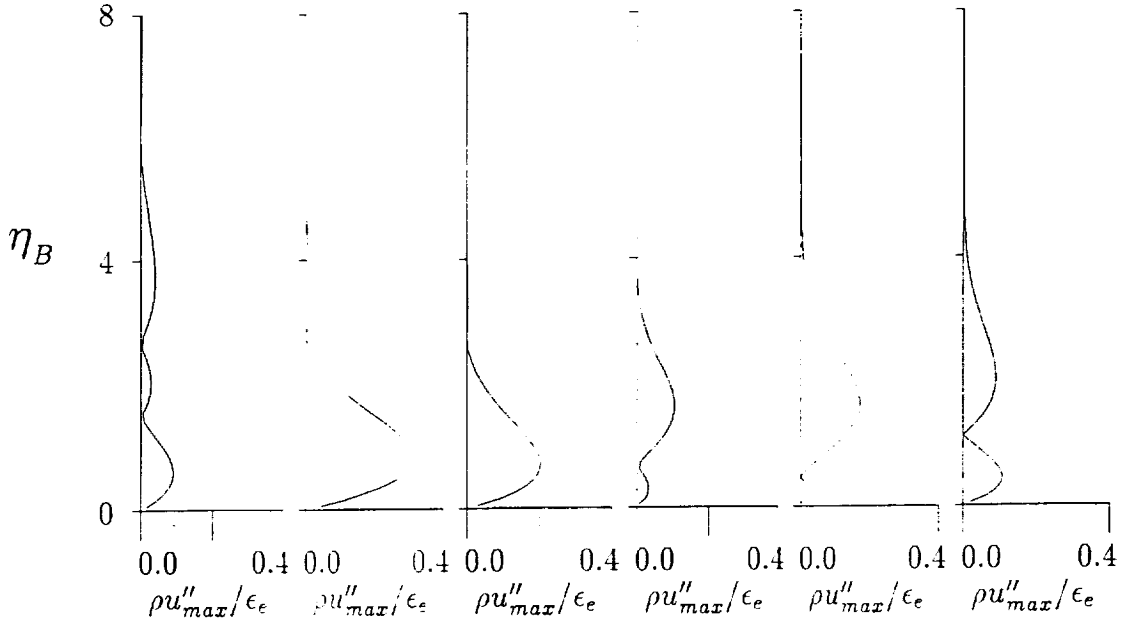

Figure 10: Maximum Streamwise Momentum Fluctuation Profiles Minus Stokes Wave for $R_n = 243$, $F = 56 \times 10^{-6}$. $0.1 \times 10^5 \leq R_s \leq 1.1 \times 10^5$

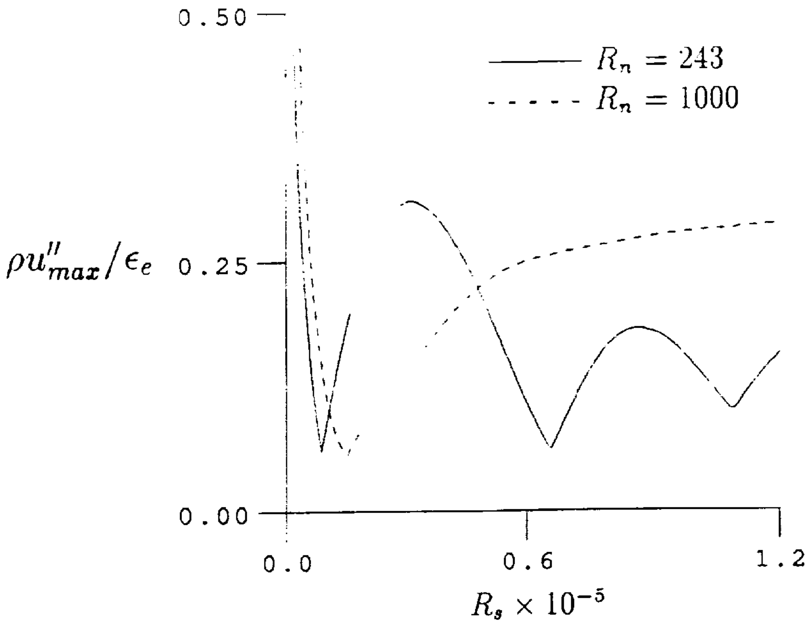

Figure 11: Maximum Streamwise Momentum Fluctuation Minus Stokes Wave vs. Reynolds Number for Different Nose Radii, $F = 56 \times 10^{-6}$

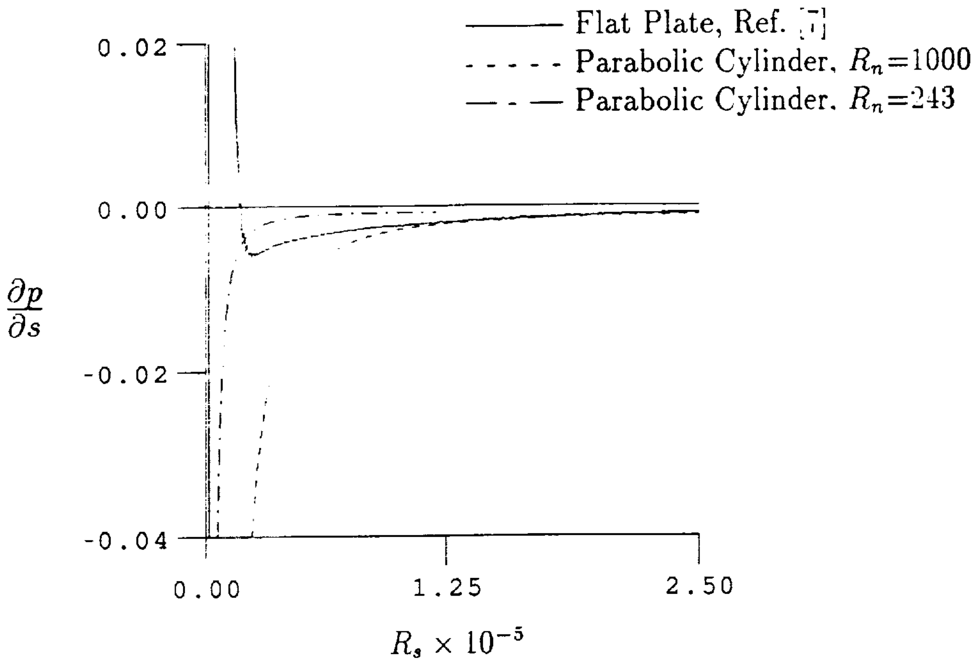

Figure 12: Mean Flow Pressure Gradient vs. Reynolds Number for Flat Plate and Parabolic Cylinder

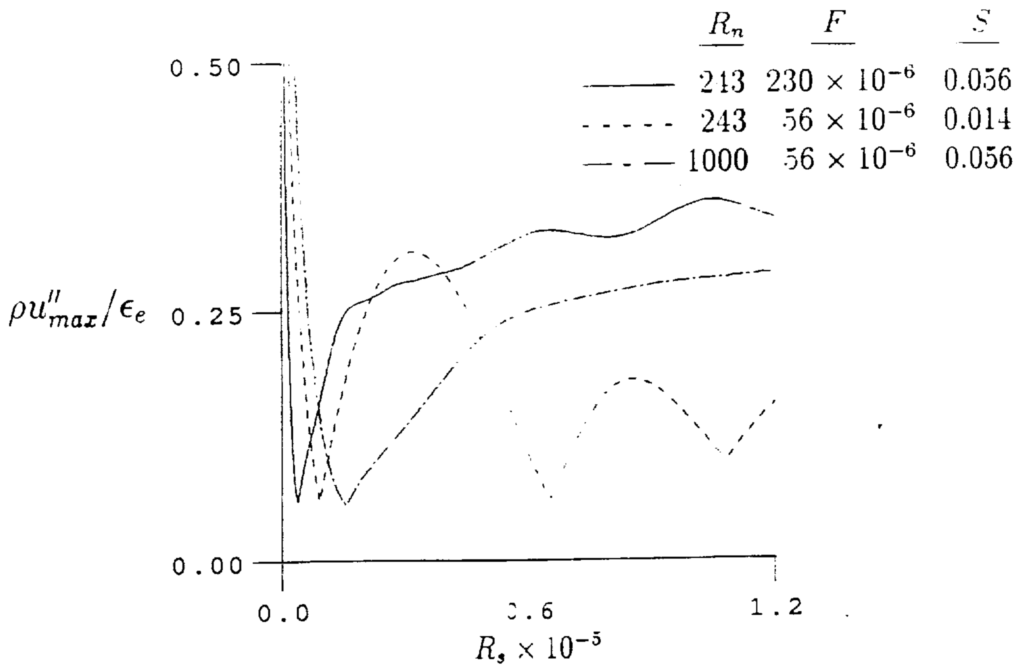

Figure 13: Maximum Streamwise Momentum Fluctuation Minus Stokes Wave vs. Reynolds Number for Various Frequencies and Nose Radii

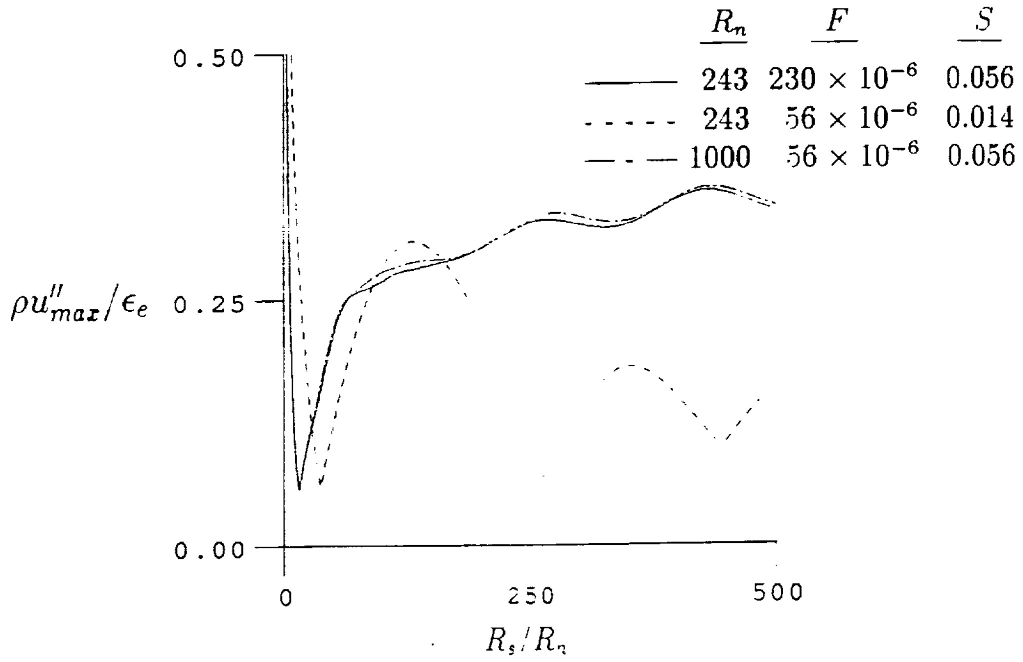

Figure 14: Maximum Streamwise Momentum Fluctuation Minus Stokes Wave vs. Reynolds Number Ratio for Various Frequencies and Nose Radii

A Transition Model for High Speed Flow

Eric S. Warren [*]
North Carolina State University, Raleigh, North Carolina
Julius E. Harris [†]
NASA Langley Research Center, Hampton, Virginia
H. A. Hassan [‡]
North Carolina State University, Raleigh, North Carolina

Abstract of Paper Proposed for the
AIAA 12th Applied Aerodynamics Conference
June 20-23, 1994
Colorado Springs, Colorado

Abstract

A transition model for low-speed flows has previously been developed by Young, et al.[1] which incorporates first-mode (Tollmien-Schlichting) disturbance information from linear stability theory. The present work extends the model to high-speed flows by incorporating the effects of second-mode disturbances. The transition model is incorporated into a Reynolds-Averaged Navier-Stokes solver with a one-equation turbulence model. Results using a variable turbulent Prandtl number approach demonstrate that the current model accurately reproduces available experimental data for first and second-mode dominated transitional flows. The performance of the present model shows significant improvement over previous transition modeling attempts.

---

[*] Research Assistant, Mechanical and Aerospace Engineering, Student Member AIAA.

[†] Senior Research Scientist, Theoretical Flow Physics Branch, Fluid Dynamics Division, Associate Fellow AIAA.

[‡] Professor, Mechanical and Aerospace Engineering, Associate Fellow AIAA.

Introduction

The study of high speed transition is very important for the efficient design of hypersonic vehicles. Hypersonic vehicles, such as the National Aerospace Plane (NASP), encounter flows which may be transitional over a significant portion of the vehicle. Within this transitional region, design parameters such as skin friction, heat transfer, etc., are rapidly increasing or are maximum. Due to the current limitations of supercomputers, the most practical method for describing such flows are methods based on the Reynolds-Averaged Navier-Stokes (RANS) equations. Traditionally, transition models based on the Reynolds-Averaged equations have consisted primarily of the modification of existing turbulence models. The main objective of this work is the development of a transition model which incorporates information from linear stability theory and accurately reproduces available experimental data for transitional flows over a wide range of Mach numbers.

At Mach numbers less than about four, the transition process is dominated by first-mode disturbances. First-mode disturbances are vorticity disturbances which are characterized by fluctuations in velocity. First-mode disturbances in incompressible flows are known as Tollmien-Schlichting waves. At Mach numbers greater than four, the transition process is dominated by second-mode disturbances. Second-mode disturbances are acoustical disturbances which are characterized by large fluctuations in pressure and temperature, fluctuations which are much larger than the velocity fluctuations.

Previous work by Young, et al.[1] has established a model for including the effects of first-mode disturbances into a transition model. The work by Young, et al.[1] dealt exclusively with incompressible flows. An objective of the present work is the extension of this model to account for Mach number effects. Additionally, the present work includes the effects of second-mode disturbances which dominate the transition process at hypersonic speeds.

Experimental Data

In order to determine the accuracy of models, it is necessary to reproduce available experimental results. In the study of natural transition, flight data or data from quiet wind tunnels is necessary. The NASA-Langley Mach 3.5 Pilot Low-Disturbance tunnel has emerged as the facility capable of reproducing transitional data of the quality that matches flight data. Using this tunnel, Chen et al.[2] presented recovery factor measurements on a 5° half-angle cone and a flat plate. Three cases from these experiments are used for comparison with the present model. These are

- Flow 3 - Case 5 $Re = 7.8e7/\mathrm{m}$ $x_t = 0.0815\mathrm{m}$
- Flow 3 - Case 6 $Re = 5.89e7/\mathrm{m}$ $x_t = 0.1174\mathrm{m}$
- Flow 3 - Case 7 $Re = 3.85e7/\mathrm{m}$ $x_t = 0.2166\mathrm{m}$

with $L_{ref} = 1m, T_{ref} = 98K, M_{ref} = 5.36, q = 0.1$[illegible]. The case designations are chosen to correspond to the same cases presented in Ref.[3]. The reference quantities given are boundary-layer edge quantities. All of the above data pertains to the cone experiments.

In order to determine the effect of the second-mode disturbances model, experiments at Mach numbers greater than four are necessary. Kimmel et al.[1] have carried out Mach 8 transition experiments over a flared and non-flared 7° half-angle cone. These experiments were carried out in the AEDC Tunnel B. The AEDC wind-tunnel is not a quiet tunnel in terms of freestream intensity levels. The freestream turbulence intensity level in the experiments[4] was around 3.0%, however, only a small portion of this was in the second-mode frequency range (frequencies above 80-100 kHz). Based on this, Ref.[5] states, "a conventional hypersonic wind tunnel can be quiet for second mode disturbances and noisy for first mode disturbances." The validity of this statement is still an open question. Regardless, at the present time, no second-mode dominated transition data obtained in quiet tunnels is available. Therefore, the present model is compared to these cases, which are given as

- Mach 8 - Flared $M = 7.98$ $Re = 6562000/\text{m}$
- Mach 8 - Non-Flared $M = 7.98$ $Re = 6562000/\text{m}$

Transition Model

If Γ represents the fraction of the time the flow is turbulent, then the mean velocity, $\vec{U}_m$ is,

$$\vec{U}_m = \Gamma \vec{U}_t + (1 - \Gamma)\vec{U}_\ell \tag{1}$$

In the above equation, $\vec{U}_t$ is the mean turbulent velocity and $\vec{U}_\ell$ is the mean non-turbulent or laminar velocity. Measurements by Kuan and Wang[3] showed that non-turbulent profiles are not Blasius profiles for flows over flat plates. Moreover, turbulent profiles are not the traditional fully developed profiles. At any given instant, the streamwise fluctuation in the transitional region, u'_r, is given by,

$$u'_r = u - U_m$$

If u is the non-turbulent velocity, then

$$u'_r = U_\ell - u'_\ell - U_m = u'_\ell - \Gamma(U_t - U_\ell)$$

and

$$\overline{u'^2_r} = \overline{u'^2_\ell} + \Gamma^2(U_t - U_\ell)^2 \tag{2}$$

Similarly, if u is the turbulent velocity, then

$$\overline{u'^2_r} = \overline{u'^2_t} + (1 - \Gamma)^2(U_t - U_\ell)^2 \tag{3}$$

ORIGINAL PAGE IS
OF POOR QUALITY

The expression given in equation (3) is obtained Γ of the time and that in equation (2), (1 − Γ) of the time. Therefore

$$\overline{u_r'^2} = \Gamma\,\overline{u_t'^2} + (1-\Gamma)\,\overline{u_\ell'^2} + \Gamma(1-\Gamma)(U_t - U_\ell)^2 \tag{4}$$

In general, one can write

$$\overline{(u_i'u_j')_r} = \Gamma\,\overline{(u_i'u_j')_t} + (1-\Gamma)\,\overline{(u_i'u_j')_\ell} + \Gamma(1-\Gamma)\,\triangle U_i\,\triangle U_j \tag{5}$$

The resulting expression is a result of three contributions: turbulent, non-turbulent, and a large-eddy component. Traditionally, transition models have only included the turbulent contribution, terms resulting from non-turbulent fluctuations have not been included. The terms $\triangle U_i \triangle U_j$ are a result of large eddies. Their calculation requires specification of the turbulent and non-turbulent profiles in the transitional region. For this work, the large-eddy term has been neglected.

The intermittency factor, Γ, is obtained from the expression developed by Dhawan and Narasimha.[5] i.e.

$$\Gamma(x) = 1 - \exp\left(-0.411\xi^2\right) \tag{6}$$

with

$$\xi = \frac{x - x_t}{\lambda}$$

and λ is determined from the correlation

$$Re_\lambda = 9\,Re_{x_t}^{.75} \tag{7}$$

x_t is value of x at the beginning of transition. Because of this, this model requires the specification of a transition "point".

Turbulent Contribution

For a fully turbulent flow, all that is needed to close the RANS equation set is the turbulent Reynolds stress, $\overline{\rho u_i'' u_j''}$ and the Reynolds heat flux, $\overline{\rho u_j'' h''}$. By evaluating the turbulent Reynolds stress, the turbulent contribution to the general transitional stress is obtained. The turbulent contribution is the first term in Eq. 5.

The turbulent Reynolds stress is given in this work by Boussinesq's approximation which gives,

$$-\overline{\rho u_i'' u_j''} = \mu_t \left(\frac{\partial \tilde{u}_i}{\partial x_j} + \frac{\partial \tilde{u}_j}{\partial x_i} - \frac{2}{3}\delta_{ij}\frac{\partial \tilde{u}_m}{\partial x_m} \right) - \frac{2}{3}\delta_{ij}\bar{\rho}\bar{k} \tag{8}$$

where μ_t is the eddy-viscosity and $\bar{k}$ is the turbulent kinetic energy per unit mass.

In this work, a one-equation model is used which specifies the eddy-viscosity as

$$\mu_t = C_\mu\,\bar{\rho}\,\sqrt{\bar{k}}\,\ell_\mu \tag{9}$$

where $C_\mu = 0.09$ is a model constant and ℓ_μ is an algebraically derived length scale. This length scale is derived by considering the near-wall behavior of k and characteristics of the log-law region in the turbulent velocity boundary layer. The turbulent viscous length scale, ℓ_μ, is given as

$$\ell_\mu = C_1 y \left[1 - \exp\left(- \frac{\sqrt{k}\, y}{C_2 \nu} \right) \right] \tag{10}$$

where

$$C_1 = (0.3)^{-\frac{3}{2}} \kappa \qquad C_2 = 70.0 \tag{11}$$

and κ is the Karman constant (0.41). The length scale ℓ_μ contains a damping factor which takes into account the presence of the laminar sublayer in the turbulent velocity profile. The form of the above length scale was originally derived by Gaffney.[7]

Reynolds Heat Flux

In the energy equation, the quantity $\overline{\rho u_j'' h''}$ appears. This term is known as the Reynolds heat flux. This term is modeled by a gradient diffusion approximation, which gives

$$\overline{\rho u_j'' h''} = - C_p\, \alpha_t\, \bar{\rho} \frac{\partial \tilde{T}}{\partial x_j} \tag{12}$$

where α_t is the turbulent diffusivity. The turbulent diffusivity can be expressed in terms of the eddy-viscosity and a turbulent Prandtl number.

$$\alpha_t = \frac{\nu_t}{Pr_t} \tag{13}$$

The resulting expression for the Reynolds heat flux becomes

$$\overline{\rho u_j'' h''} = - \frac{C_p \mu_t}{Pr_t} \frac{\partial \tilde{T}}{\partial x_j} \tag{14}$$

where C_p is the specific heat at constant pressure, μ_t is the eddy viscosity, and Pr_t is the turbulent Prandtl number.

Traditionally, the turbulent Prandtl number is taken as a constant. The value of Pr_t varies in the literature but generally is chosen between 0.8 and 1.0. In this work, when the turbulent Prandtl number is chosen as a constant, the value is taken as 0.89. This was chosen to correspond to the value used in reference [3].

There are physical consequences in choosing Pr_t as a constant. By examining Eq. 14, it is clear that when Pr_t is a constant, the damping factor used is the same factor which appears in ℓ_μ. This is equivalent to treating the turbulent thermal boundary layer with the same damping as the turbulent velocity boundary layer, even though they have different laminar sublayer characteristics. As results will illustrate, this choice has surprising consequences when considering quantities which are strong functions of the Prandtl number, such as the recovery factor.

Eddy-Diffusivity Model

It is possible to model the Reynolds heat flux in such a way that the turbulent temperature boundary layer is damped differently than the turbulent velocity boundary layer. Based on the variable turbulent Prandtl number approach of Cebeci.[8] the eddy-diffusivity model is assumed to have the form

$$\alpha_t = C_\mu \sqrt{\bar{k}}\, \ell_T \tag{15}$$

The temperature length scale, ℓ_T, is assumed similar in form to the viscous and dissipation length scales and is given as.

$$\ell_T = C_3\, y \left[1 - \exp\left(-\frac{\sqrt{\bar{k}}\, y}{C_4\, \nu} \right) \right] \tag{16}$$

where

$$\begin{aligned} C_3 &= 3.12 \\ C_4 &= 92.0 \end{aligned}$$

The constants C_3 and C_4 were determined by comparing with the experimental turbulent Prandtl number measurements of Meir and Rotta.[9]

By defining a separate length scale for the temperature boundary layer, different damping is obtained. The present eddy-diffusivity model implies a variable turbulent Prandtl number of the form.

$$Pr_t = \frac{\ell_\mu}{\ell_T} \tag{17}$$

where ℓ_μ is the viscous length scale.

Non-Turbulent Fluctuations

The second term in the general transitional stress.

$$(1 - \Gamma)\, \overline{\left(u_i' u_j' \right)_l} \tag{18}$$

is a result of laminar or non-turbulent fluctuations. As stated previously, this non-turbulent contribution has traditionally not been considered in RANS-type approaches. In this work, the non-turbulent fluctuations considered are a result of first and second-mode disturbances.

First-Mode Disturbances

For moderate supersonic Mach numbers below approximately four, the dominant mode of instability is the first mode. The dominant disturbance frequency at breakdown is well predicted by the frequency of the first-mode disturbance having the maximum amplification rate. Using the work of Obremski et al.,[10] Walker[11] states that this frequency can be correlated by

$$\frac{\omega\nu}{U_e^2} = 3.2\, Re_{\delta^*}^{-\frac{3}{2}} \tag{19}$$

where U_e is the velocity at the edge of the boundary layer. Re_{δ^*} is the Reynolds number based on displacement thickness, δ^*, and ω is the frequency.

The above expression is valid for low speed flow but can be extended, through the use of the reference temperature method, to high speed flow. It is known[12] that compressible formulas for skin friction and heat transfer have the same form as the incompressible formulas provided the physical properties of the fluid are evaluated at some reference temperature between T_w and T_e. A possible definition of T^* is[13]

$$\frac{T^*}{T_e} = 1 + 0.032\, M_e^2 + 0.58\left(\frac{T_w}{T_e} - 1\right) \tag{20}$$

where the e subscript denotes boundary-layer edge quantities and w denotes wall values. By using this reference temperature, Walker's formula, i.e. Eq. 19, can be extended to higher Mach number flows by considering the definition of the unit Reynolds number as

$$Re^* = \frac{\rho^* U_\infty}{\mu^*} \tag{21}$$

with

$$\mu^* = \mu(T^*) \tag{22}$$

where T^* is the reference temperature evaluated from Eq. 20. The density can be approximated by noting

$$\frac{P_e}{P^*} = \frac{\rho_e\, R\, T_e}{\rho^*\, R\, T^*}$$

and assuming that the pressure is approximately constant throughout the boundary layer.

$$\frac{\rho^*}{\rho_e} = \frac{T_e}{T^*} \tag{23}$$

The dominant first-mode frequency correlation can then be rewritten as

$$\frac{\omega\nu^*}{U_e^2} = 3.2\,(Re^*_{\delta^*})^{-\frac{3}{2}} \tag{24}$$

with δ^* also evaluated using Re^*.

By assuming a scale of $\sqrt{k}$, the first-mode disturbance frequency ω can be used to define a length scale.

$$\ell_{TS} = a\,\frac{\sqrt{k}}{\omega} \qquad a = 0.04 - 0.06 \tag{25}$$

It is assumed that the turbulent and non-turbulent contributions to the stress tensor can be obtained by combining the two length scales as

$$\ell_\mu = (1-\Gamma)\ell_{TS} + \Gamma \ell_\mu^t \tag{26}$$

where ℓ_μ^t is the turbulent viscosity length scale. Thus, when $\Gamma = 0$, i.e. before transition

$$\ell_\mu = \ell_{TS}$$

Second-Mode Disturbances

Through the pioneering work of Mack,[14, 15] the concept of second-mode disturbances was developed. As the boundary layer edge velocity increases above approximately $M = 2.2$, a region of the boundary layer becomes supersonic relative to the phase velocity. Mack showed that when such a situation exists, multiple solutions to the inviscid stability equations arise. These additional solutions are called the higher modes. The first of these modes is called the second-mode and is the most unstable of the higher modes, sometimes referred to as the Mack modes.

At relatively low Mach numbers, boundary layer transition is dominated by lower frequency first mode disturbances. As the Mach number increases above four, the second-mode disturbances, which are higher frequency acoustical disturbances, dominate the transition process. From Mack[16] and Stetson and Kimmel,[5] the wave lengths of the most unstable second-mode disturbances have been shown to be about two boundary layer thicknesses.

The frequency of the second mode disturbances can be written as

$$\omega_{2M} = \frac{U_p}{\lambda} \tag{27}$$

where U_p is the phase velocity and λ is the wavelength. For hypersonic boundary layers, this leads to the relationship

$$\lambda \propto 2\delta = \frac{c M_e^2 x}{\sqrt{Re_x}} \tag{28}$$

where c is a constant of proportionality. Combining with Eq. 27, the frequency is given as

$$\omega = \frac{U_p \sqrt{Re_x}}{c M_e^2 x} \tag{29}$$

Again defining a velocity scale as in Eq. 25, a second-mode contribution to the length scale can be defined as

$$\ell_{2M} = b\frac{\sqrt{\tilde{k}}}{\omega}$$

which upon substitution of Eq. 29 above, yields

$$\ell_{2M} = \left(\frac{b}{U_p}\right) M_e^2 \sqrt{\frac{\tilde{k}\, x}{Re}} \tag{30}$$

By comparing with the Mach 8 stability experiment of Kimmel,[1,17] the constant δ was chosen as 0.23. Additionally, linear stability predicts the phase velocity to be about $0.94 U_\infty$. Again, it is assumed that the second-mode contribution can be obtained by combining ℓ_{SM} into the viscous length scale giving

$$\ell_\mu = (1-\Gamma)\left[\ell_{TS} + \ell_{SM}\right] + \Gamma \ell_\mu^T \tag{31}$$

Results and Discussion

Numerical Method

The numerical method used to solve the equation set follows the method of Ref. [7] closely. A finite-volume method was used to evaluate the spatial terms in the Navier-Stokes equations. The inviscid fluxes were computed by an upwind approach based on Roe's flux difference splitting. MUSCL differencing was used along with a min-mod flux limiter. Second-order central differencing was used to evaluate the viscous fluxes. The solution was stepped in time using a modified four-stage Runge-Kutta scheme until a steady-state was obtained. The determination of a steady-state was based on a density residual drop of five or more orders of magnitude. Due to the existence of a shock, grids of approximately 275x75 were needed to adequately resolve the shock and the very thin boundary-layer region. The steady-state was obtained with run-times on the average of 3-4 Cray Y-MP hours.

Due to the very large Reynolds numbers, as high as 8×10^7, the thin-layer Navier-Stokes equations were solved. The thin-layer approximation neglects streamwise derivatives in the viscous terms due to their small magnitude relative to the normal derivatives. This is a valid approximation since at very large Reynolds numbers the viscous effects are restricted to a very small region near a solid boundary. Due to the cell aspect ratios necessary to resolve this small region, streamwise derivatives in the viscous terms have a negligible contribution.

Mach 3.5 Cases

The Mach 3.5 cases were used to determine the effectiveness of the transition model at predicting transitional flows which are characterized by first-mode dominated transition processes. Previous work by Young et al.[1] has established the capability of the model for low-speed flat plate flows. The Mach 3.5 cases studied were the ones carried out on the 5° half-angle cone. A flat plate case was also studied but was not presented here. The cone experiments measured the recovery factor by determining the surface temperature under adiabatic conditions.

The first set of results were obtained with the present model using a constant turbulent Prandtl number. The experiment data is from the Flow 3 - Case 5 experiment which is the first experiment of the Chen et al.[2] set. Fig. 1 compares the present model with the linear combination models of Narasimha and ONERA/CERT. Linear combination models assume the viscosity can be expressed as

$$\mu = \mu_l + \Gamma \mu_t \tag{32}$$

The curve labeled Narasimha used the expression for Γ given by Eq. 6 while the ONERA/CERT model is based on a transition function, ϵ_t, which replaces Γ in the above expression. This transition function, ϵ_t, is empirically derived and is discussed in Ref. [3]. Fig. 1 is a plot of recovery factor versus Reynolds number based on the distance along the surface. Fig. 1 demonstrates that the present model does a much better job of predicting the length of the transition zone as well as the peak in the recovery factor. The laminar region is also predicted well. The Narasimha and ONERA/CERT models were computed with a boundary layer code and not a Navier-Stokes formulation. It is believed that the boundary layer codes were started with a laminar profile just before the transition region and therefore the laminar region was never calculated. The recovery factor was assumed to be $\sqrt{Pr}$ and thus resulted in a straight line for the linear combination models. Both the linear combination models and the present constant Pr_t model do a poor job of reproducing the decreasing trend of the recovery factor in the fully turbulent region.

Fig. 2 compares the present results of the constant turbulent Prandtl number model to the two-equation transition model of Wilcox.[17] The Wilcox model modifies the production and dissipation terms in the k-ω turbulence model to simulate transition. The Wilcox model does a better job of reproducing the peak in the recovery factor than the linear combination models. However, the present model with a constant Pr_t does a slightly better job than the Wilcox model in calculating the recovery factor peak and does a much better job reproducing the transition extent. Additionally, the present method does a slightly better job in the fully turbulent region, although both fail to predict the downward trend in the recovery factor.

The calculation of recovery factor is very sensitive to the choice of the turbulent Prandtl number. Fig. 3 is a plot of the current transition model with various choices of the constant Pr_t. By varying the choice of Pr_t by as little as 0.01, very large differences result in the calculation of the recovery factor. This is not too surprising since the recovery factor is such a strong function of the Prandtl number. In Fig. 3, the solid line represents the choice of $Pr_t = 0.89$ which is the choice used for the linear combination models as described in Ref. [3].

Since the recovery factor is sensitive to the value of Pr_t, a closer look was taken at modeling the turbulent diffusivity. As stated previously, using a constant turbulent Prandtl number effectively treats the damping of the thermal boundary layer exactly the same as the damping of the velocity boundary layer. This has no physical basis, especially for high-speed flows where the thermal boundary layer becomes important due to the large temperature gradients in the viscous layer. Following the work of Cebeci,[3] the concept of a variable turbulent Prandtl number was used to define the current eddy-diffusivity model (Eq. 15). A typical profile of the variable turbulent Prandtl number is compared in Fig. 8 to the flat-plate measurements of Meir and Rotta.[9] The results of this model for the Flow 3, Case 5 experiment are shown in Fig. 4. As can be seen from the figure, the experimental data in the turbulent region is almost exactly reproduced. Even though the peak in the recovery factor is slightly overpredicted, the transition extent is predicted very well.

To determine if the constants used in the specification of the temperature length scale, Eq. 16, are general, the other experiments in the Mach 3.5 cases were computed. Fig. 5 is the results of the present model for the second case. Flow 3 - Case 6. It is clear that the present model accurately reproduces the transition extent, the peak in the recovery factor, and the turbulent region. The results show the extreme differences in the predictions of the present method and the linear combination models. A curious observation in the laminar region can be seen by examining Fig. 5. The experimental data is almost flat in the laminar region while the present method predicts a slight increase in the recovery factor. The experimental results shown here were obtained with the same test model as were the results in Fig. 4. However, different values were measured for the recovery factor for the same Reynolds number based on x. This seems to suggest either slight error in the measurements or the existence of some external phenomena. Fig. 6 is the results for the Flow 3 - Case 7. Even though the transition extent is predicted well, poorer results are obtained in comparison with the other two cases. There is a possible explanation for this. Each of the experiments were carried out with the same test model. A reasonable assumption is that the recovery factor measured should be the same for each of the test cases for the same Re_x, given that laminar flow exists there. Fig. 7 demonstrates that each of the cases measured different values for the laminar recovery factor at the same Re_x. As seen from the figure, the Flow 3 - Case 5 experiment measured around 0.837 for the recovery factor, while each of the succeeding cases measured values of about 0.840 and 0.844 respectively. This is clearly a discrepancy in the data. If the tests were not allowed to completely reach steady-state (adiabatic wall conditions), the measured value of the recovery factor would have been higher than the steady-state value. Since the computations assumed adiabatic conditions, and consistent values for the recovery factor were computed in the laminar region, it is possible that the present method accurately predicts the steady-state value of the recovery factor for the laminar, transitional, and turbulent regions.

The transitional results presented by Chen et al.[2] are well predicted by the present model. Moreover, the results of the current model illustrate the inadequacies of using a constant turbulent Prandtl number for cases that present recovery factor data. Evidently, the current transition model is the only model presently known, that correctly reproduces the trend in the turbulent region for these experiments.[3, 17]

Mach 8 Cases

The Mach 8 cases were used to determine the effectiveness of the present model in predicting transitional flows which are characterized by second-mode dominated transition processes. The experiments were carried out by Kenneth Stetson and Roger Kimmel at the AEDC (Arnold Engineering Development Center) tunnel B and were reported in Ref. [4].

The first case considered is the flared cone case. The surface is flared to produce a constant adverse pressure gradient. Fig. 9 presents the results for the present model without the second-mode contribution given in Eq. 31. The results are presented as the dimensional surface heat flux versus distance along the surface. The laminar and the fully turbulent region are slightly underpredicted for this case. Fig. 10 shows the same results for the present transition model with the second-mode contribution. With this second-mode contribution.

the laminar data is predicted correctly. However, the fully-turbulent region is still underpredicted. Since the surface was cooled, it was determined that the modeled near-wall behavior of the turbulent kinetic energy, given in Ref. [7, Appendix D], needed modification. A factor of $\sqrt{\frac{T_w}{T_{aw}}}$ was used in the present model to include effects of wall temperature and to account for the fact that the near-wall behavior was originally modeled in Ref. [7] for adiabatic flows. The inclusion of this factor results in the following expression for the constant which appears in the turbulent viscous length scale (Eq. 10).

$$C_2 = 70.0\sqrt{\frac{T_w}{T_{aw}}} \tag{33}$$

Fig. 11 is the results of the present model with the near-wall modification. The experimental data is reproduced very well. The experimental data seems to imply that the heat flux in the turbulent region is either flat or is decreasing. This seems to be reinforced by the calculations in Ref. [17]. However, Kimmel[4] points out that, "An adverse pressure gradient in incompressible flow causes boundary layer thickness to increase and heat transfer to decrease compared to zero-pressure gradient values, but the opposite trends occur in compressible flow. This is primarily because of changes in streamtube size and Mach number in pressure gradients in compressible flow. Consequently, wall shear and heat transfer decrease more slowly with x in an adverse pressure gradient than in zero pressure gradient. A strong enough adverse gradient causes heat transfer and wall shear to increase in the x-direction." Additionally, Kimmel[4] states that the error in the measurements could have been as high as ±10%. It is therefore possible that the increase in the heat transfer shown by the present method in the turbulent region is accurate.

The second case of the Mach 8 experiments was the non-flared 7° half-angle cone. Fig. 12 presents the results of the current transitional model with the second-mode contribution as well as the near-wall modification. The results are presented as non-dimensional heat flux versus non-dimensional distance along the surface. The transitional and turbulent regions are reproduced quite well. The discrepancy in the laminar region is most likely experimental error since there is large scatter and no clear transition point. It is also possible that the laminar discrepancy is a result of the high levels of freestream turbulence.

As the comparisons with the hypersonic cases demonstrate, the second-mode model performs quite well.

Conclusions

The present transition model is based on the fact that the stress in the transitional region can be expressed as a function of the turbulent and non-turbulent stresses. The non-turbulent stress is due to the presence of laminar fluctuations which are a result of first and second-mode oscillations. This work has successfully formulated a method in which these laminar disturbances can be accounted for in the computation of a high-speed transitional flow. The previous work of Young et al.[1] has demonstrated the effectiveness of the first-mode

ORIGINAL PAGE IS
OF POOR QUALITY

contribution for low-speed flows. The present work demonstrates that the model can be extended to high-speed flows through the use of the reference temperature method.

The present work successfully demonstrates that second-mode disturbances can also be included into the transition model using a form similar to the first-mode disturbance model. The resulting transition model accurately reproduces available experimental data for transitional flows. The model has been shown to predict first-mode dominated transitional flows very accurately and performed better than previous modeling attempts. Additionally, the model has been shown to accurately predict hypersonic transitional flows which are characterized by second-mode dominated transition.

References

[1] Young, T. W., Warren, E. S., Harris, J.E., and Hassan, H. A. "New Approach for the Calculation of Transitional Flows". *AIAA Journal*, Vol. 31(4):629–636, Apr. 1993.

[2] Chen, F.-J., Malik, M. R., and Beckwith, I. E. "Boundary-Layer Transition on a Cone and Flat Plate at Mach 3.5". *AIAA Journal*, Vol. 27(6):687–693, June 1989.

[3] Singer, B. A., Dinavahi, S. P. G., and Iyer, V. "Testing of Transition-Region Models: Test Cases and Data". NASA Contractor Report 4371, May 1991.

[4] Kimmel, R. L. "Experimental Transition Zone Lengths in Pressure Gradient in Hypersonic Flow". In Kral, L. D., and Zang, T., editor, *Symposium on Transitional and Turbulent Compressible Flows*, volume FED 151, pages 117–127. ASME Fluids Engineering Conf., 1993.

[5] Stetson, K. F., and Kimmel, R. L. "On Hypersonic Boundary-Layer Stability". AIAA Paper 92-0737, 1992.

[6] Dhawan, S. and Narasimha, R. "Some Properties of Boundary Layer Flow During Transition from Laminar to Turbulent Motion". *Journal of Fluid Mechanics*, 3(4):418–436, 1958.

[7] Gaffney, R. L. *An Abbreviated Reynolds Stress Turbulence Model for Airfoil Flows*. PhD thesis, North Carolina State University, 1990.

[8] Cebeci, T. "A Model for Eddy Conductivity and Turbulent Prandtl Number". *J. Heat Transfer*, pages 227–233, May 1973.

[9] Meier, H. U., and Rotta, J. C. "Temperature Distributions in Supersonic Turbulent Boundary Layers". *AIAA Journal*, Vol. 9(11):2149–2156, Nov. 1971.

[10] Obremski, H. J., Morkovin, M. V., and Landahl, M. "Portfolio of Stability Characteristics of Incompressible Boundary Layers". AGARDograph 134, Mar. 1969.

[11] Walker. G. J. "Transitional Flow on Axial Turbomachine Blading". *AIAA Journal.* Vol. 27(5):595–602. May 1989.

[12] Anderson. J. D.. Jr. *Hypersonic and High Temperature Gas Dynamics.* McGraw-Hill. 1989.

[13] Eckert. E. R. G. "Engineering Relations for Heat Transfer and Friction in High-Velocity Laminar and Turbulent Boundary-Layer Flow Over Surfaces with Constant Pressure and Temperature". *Trans. of the ASME.* Vol. 78(6):1273. Aug. 1956.

[14] Mack. L. M. "Linear Stability Theory and the Problem of Supersonic Boundary-Layer Transition". *AIAA Journal.* Vol. 13(3):278–289. Mar. 1975.

[15] Mack. L. M. "Boundary Layer Linear Stability Theory". AGARD Report No. 709. June 1986.

[16] Mack. L. M. "Stability of Axisymmetric Boundary Layers on Sharp Cones at Hypersonic Mach Numbers". AIAA Paper 87-1413. 1987.

[17] Chang, C.-L.. Singer. B. A.. Dinavahi. S. P. G.. El-Hady. N. M.. Harris. J. E.. Streett, C. L.. and Wilcox. D. C. "Transition Region Modeling for Compressible Flow". NASP Contractor Report 1142, Feb. 1993.

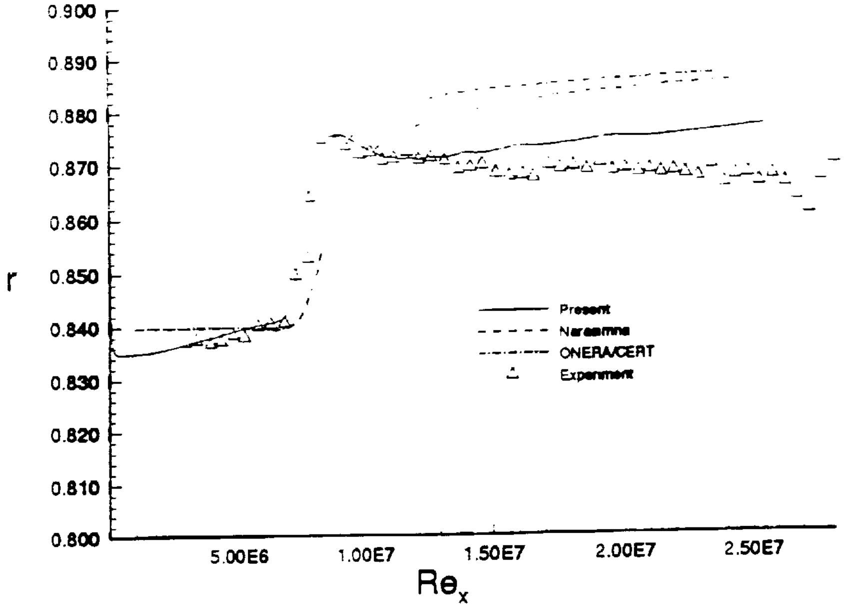

Figure 1. Flow 3 - Case 5. Constant Pr_t vs. Previous Linear Combination Models

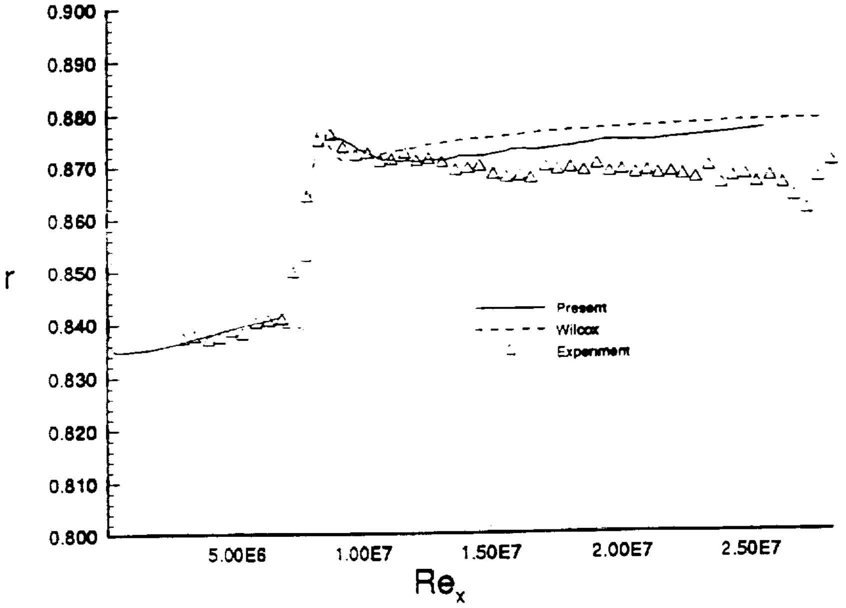

Figure 2. Flow 3 - Case 5. Constant Pr_t Case vs. Wilcox Model

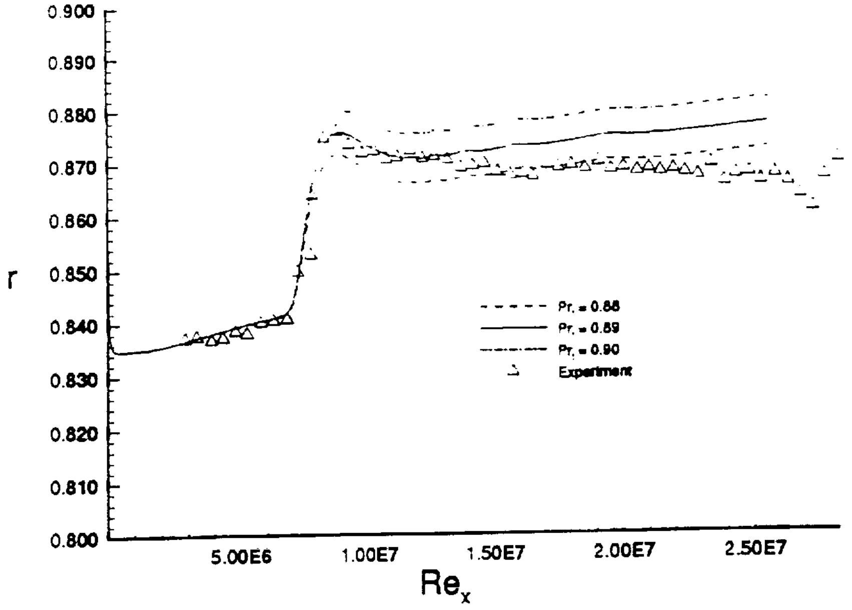

Figure 3. Flow 3 - Case 5. Turbulent Prandtl Number Sensitivity

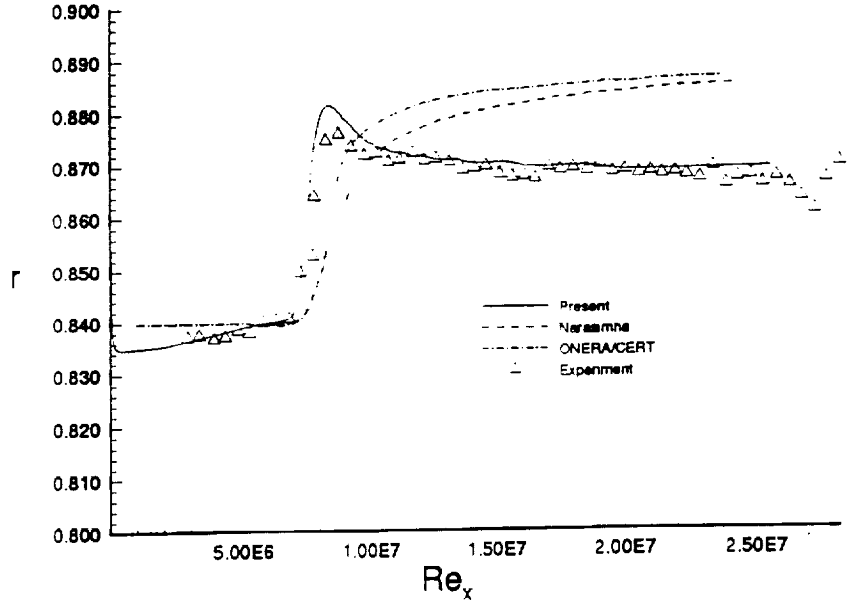

Figure 4. Flow 3 - Case 5. One-Equation Eddy Diffusivity Model Comparison

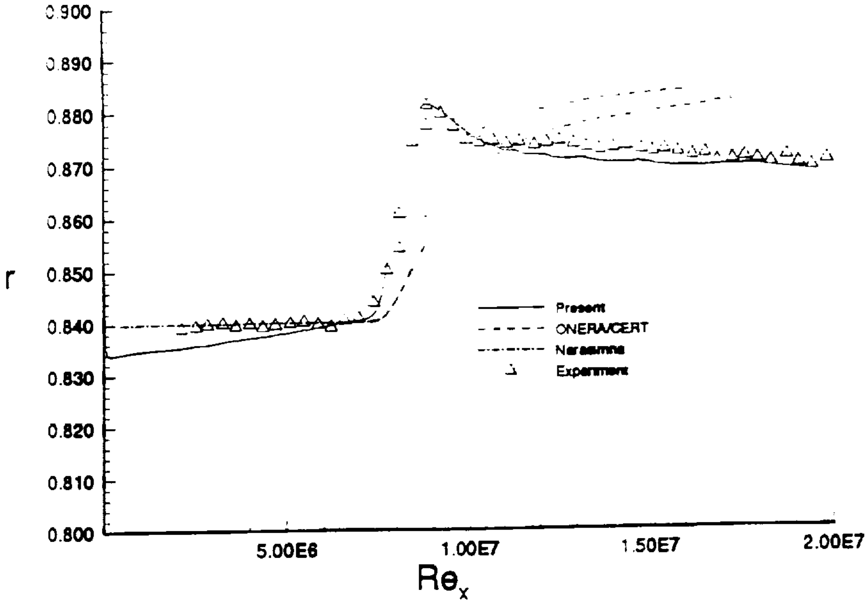

Figure 5. Flow 3 - Case 6, One-Equation Eddy Diffusivity Model Comparison

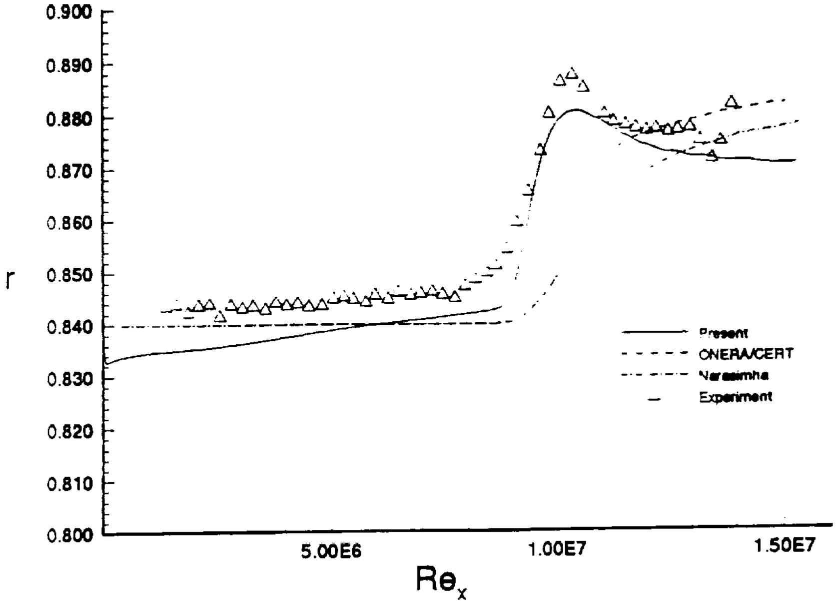

Figure 6. Flow 3 - Case 7, One-Equation Eddy Diffusivity Model Comparison

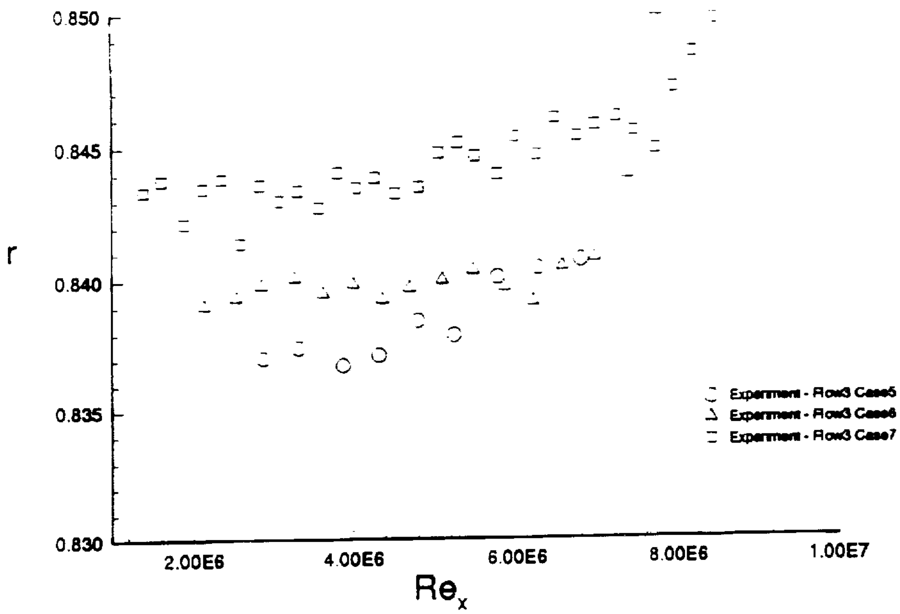

Figure 7. Flow 3. Comparison of Measured Recovery Factor (Laminar)

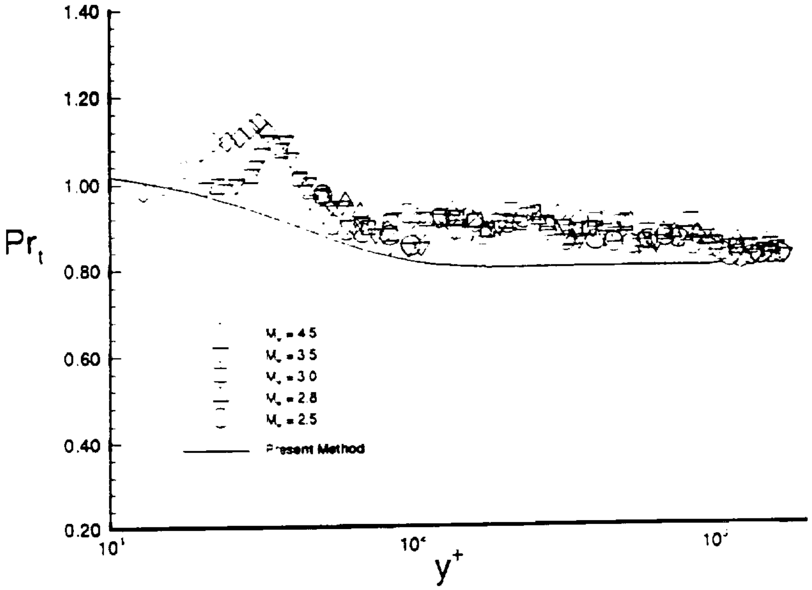

Figure 8. Experimental Pr_t Measurements of Meir and Rotta

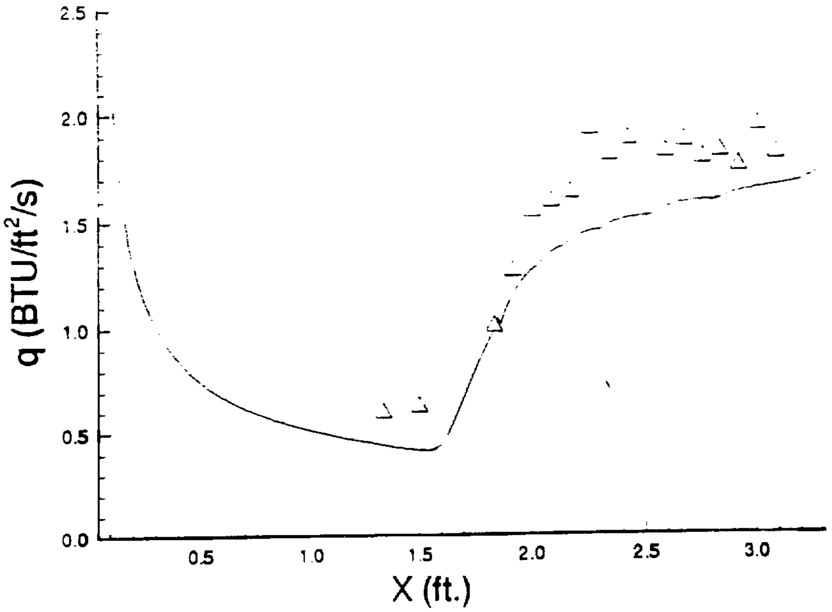

Figure 9. Mach 8 - Flared Cone. Present Method Without Second-Mode Model

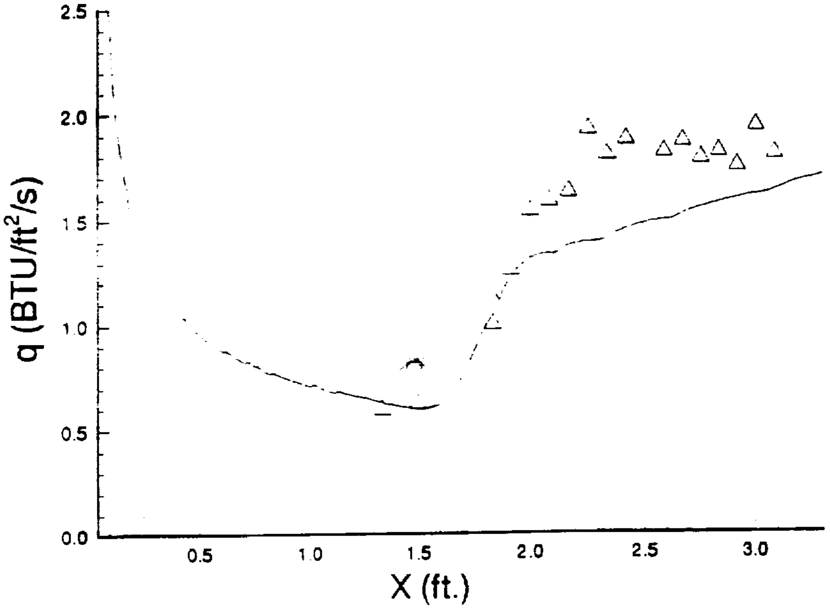

Figure 10. Mach 8 - Flared Cone. Present Method With Second-Mode Model